

Thomas Kirchartz | José A. Márquez | Martin Stolterfoht | Thomas Unold

Photoluminescence-based characterization of halide perovskites for photovoltaics

Suggested citation referring to the original publication:

Advanced Energy Materials 10 (2020) 26, Art. 1904134 pp. 1 - 21

DOI <https://doi.org/10.1002/aenm.201904134>

ISSN 1614-6832, 1614-6840

Journal article | Version of record

Secondary publication archived on the Publication Server of the University of Potsdam:

Zweitveröffentlichungen der Universität Potsdam : Mathematisch-Naturwissenschaftliche Reihe 1419

ISSN: 1866-8372

<https://nbn-resolving.org/urn:nbn:de:koby:517-opus4-519702>

DOI: <https://doi.org/10.25932/publishup-51970>

Terms of use:

This work is licensed under a Creative Commons License. This does not apply to quoted content from other authors. To view a copy of this license visit <https://creativecommons.org/licenses/by/4.0/>.

Photoluminescence-Based Characterization of Halide Perovskites for Photovoltaics

Thomas Kirchartz,* José A. Márquez, Martin Stolterfoht, and Thomas Unold*

Photoluminescence spectroscopy is a widely applied characterization technique for semiconductor materials in general and halide perovskite solar cell materials in particular. It can give direct information on the recombination kinetics and processes as well as the internal electrochemical potential of free charge carriers in single semiconductor layers, layer stacks with transport layers, and complete solar cells. The correct evaluation and interpretation of photoluminescence requires the consideration of proper excitation conditions, calibration and application of the appropriate approximations to the rather complex theory, which includes radiative recombination, non-radiative recombination, interface recombination, charge transfer, and photon recycling. In this article, an overview is given of the theory and application to specific halide perovskite compositions, illustrating the variables that should be considered when applying photoluminescence analysis in these materials.

hole transport layers (TLs) and metal or metal-oxide electrodes. The simple processing allowed rapid variation of various parameters regarding the absorber and interfaces to the transport layers that led to remarkably fast improvements in the reduction of non-radiative recombination losses and consequently efficiency.^[4–7] One of the key experimental methods to better understand recombination and to quantify losses in the bulk and at different interfaces has been photoluminescence (PL).^[8,9] To date a broad range of PL measurement techniques/methodologies have been proposed to study perovskite films and solar cells, including temperature,^[10–12] fluence,^[9,13] and voltage-dependent^[14] as well as spatially^[15,16] and time-resolved

1. Introduction

Halide perovskite solar cells have reached power conversion efficiencies exceeding 25%, that is, more than any other thin-film technology except for GaAs.^[1] A key to achieve this has been the ability to use relatively simple processing technologies^[2,3] based mostly on solution chemistry to fabricate thin layers of halide-perovskite absorbers sandwiched between electron and


PL.^[8,17,18] Steady-state PL measurements, for example, have been used to identify the limiting interfaces and/or components of the complete cell.^[8,9,19] Temperature-dependent PL has been used to identify the distribution of trap states at low temperatures, phase transitions, and different perovskite crystal structures.^[10,20,21] Intensity-dependent measurements have, for example, improved the understanding of the ideality factor as well as the internal and the external voltage, especially at high light intensities where the open-circuit voltage can saturate due to increased surface recombination or other effects.^[9,13] In addition, the voltage-dependent PL from a complete cell has been used to understand the interplay between radiative and non-radiative recombination as well as the internal and external voltage in the power generating JV-regime, especially in the presence of low-resistive transport layers.^[14] Moreover, hyperspectral or confocal PL imaging is a powerful tool to study microscopic and large area inhomogeneities which are relevant for devices.^[16] Steady-state PL measurements have been used to study the movement of different ionic species which may quench or enhance the PL over long timescales ($>s$).^[22,23] Finally, transient PL is a very popular tool to reveal the kinetics of charge transfer and/or recombination on ns-timescales allowing us to quantify, for example, the key recombination rate constants of trap-assisted Shockley–Read–Hall (SRH), bimolecular, and Auger recombination.^[24,25] These parameters have been subsequently used in global drift-diffusion simulations to model complete solar cells in steady-state.^[26,27] However, to date there remain many inconsistencies and different interpretations about the importance of certain physical processes or recombination mechanisms, which is likely due to the rather large number of different perovskite compositions and characterization methodologies that have been proposed over the last years. For any

Prof. T. Kirchartz
IEK5-Photovoltaik
Forschungszentrum Jülich
Jülich 52425, Germany
E-mail: t.kirchartz@fz-juelich.de

Prof. T. Kirchartz
Faculty of Engineering and CENIDE
University of Duisburg-Essen
Carl-Benz-Str. 199, Duisburg 47057, Germany

Dr. J. A. Márquez, Dr. T. Unold
Department of Structure and Dynamics of Energy Materials
Helmholtz-Zentrum-Berlin
Hahn-Meitner-Platz 1, Berlin 14109, Germany
E-mail: unold@helmholtz-berlin.de

Dr. M. Stolterfoht
Institute of Physics and Astronomy
University of Potsdam
Carl-Liebknecht-Str. 24–25, Potsdam-Golm D-14476, Germany

 The ORCID identification number(s) for the author(s) of this article can be found under <https://doi.org/10.1002/aenm.201904134>.

© 2020 The Authors. Published by WILEY-VCH Verlag GmbH & Co. KGaA, Weinheim. This is an open access article under the terms of the Creative Commons Attribution License, which permits use, distribution and reproduction in any medium, provided the original work is properly cited.

DOI: 10.1002/aenm.201904134

photovoltaic material system, technological maturity has to come with an improved understanding of the key physical processes and especially the key remaining loss processes.^[5] Hence, the tools to study these processes and losses themselves have to be well understood and their application to particular sample types or devices has to rely on a solid theoretical base needed to correctly interpret and quantify the resulting experimental data. While both steady-state and transient photoluminescence spectroscopy have been frequently used in the community to study recombination processes in films and devices and a number of good overviews on photoluminescence theory of photovoltaic materials have been published previously,^[28,29] the results of these experiments are partly quite challenging to understand and the analysis methods, especially for transient photoluminescence, often require complex numerical techniques.^[30] For example, the quenching of the PL of a neat material by a transport layer (TL) is often used to quantify charge transfer^[31,32] or to demonstrate the superior charge-extraction properties of new TLs. Moreover, kinetic parameters are usually not correlated to bulk- and interfacial-recombination losses in steady-state, and there exists a large spread in reported recombination parameters for specific perovskite compositions in the literature. As a consequence, it is presently quite unclear in the community, how certain kinetic properties in the bulk or the interfaces correlate to the open-circuit voltage or other performance parameters in steady-state.

The present tutorial focuses on the two different measurement types as presented in **Figure 1** and discusses how the data analysis becomes increasingly complex depending on the number of charge-extracting interfaces within the investigated sample. We first focus on the more complex technique of transient photoluminescence; in particular on the impact of various recombination processes in the bulk and the interfaces as well as photon recycling on the decay dynamics of the PL signal. We then discuss how these measurements can be complemented by steady-state photoluminescence and measurements of the open-circuit voltage of complete solar cells. Finally, we discuss how charge-carrier recombination and/or transfer processes as obtained from transient PL measurements relate to the non-radiative recombination losses in the bulk and the interfaces and we discuss recent developments in the literature in this regard.

2. Experimental Setups

Various experimental setups can be used to measure photoluminescence in thin film semiconductors and also in complete solar cell layer stacks. Here, a brief overview will be given on the most common methods used and the literature will be referred to for more detailed discussion.

2.1. Time Resolved Photoluminescence

A common method to record transient photoluminescence signals is the so-called time-correlated single photon counting technique. A general sketch of a typical setup is shown in **Figure 2**. Here, a single-photon sensitive detector, such as an



Thomas Kirchartz is a professor in the department of Electrical Engineering and Information Technology at the University Duisburg-Essen (since 2013). In addition, he is the head of the department of *Analytics and Simulation* and the group for *Organic and Hybrid Solar Cells* at the Research Centre Jülich (Institute for Energy and

Climate Research). Previously he was a Junior Research Fellow at Imperial College London (2010–2013) and received a Dr.-Ing. from RWTH Aachen (2009). His research interests include the fundamental understanding of photovoltaic devices, their characterization and simulation and the development of solution-processable solar cells.



José A. Márquez is currently working as a Post-Doc researcher in the Structure and Dynamics of Energy Materials Department at the Helmholtz-Zentrum Berlin (HZB). He graduated in chemistry at the University of Sevilla and completed his PhD in physics and electrical engineering at Northumbria University as part of a Marie Curie

Programme. His PhD included research stays at HZB and at EMPA in the Laboratory for Thin Films and Photovoltaics developing earth-abundant semiconductors for photovoltaics. His current research focuses on the development of novel compound semiconductors and high-throughput and *in-situ* characterization methods for energy materials.



Thomas Unold leads the *Combinatorial Energy Materials Research* group in the Department Structure and Dynamics of Energy Materials at the Helmholtz-Zentrum Berlin (HZB). The group currently focuses on the exploration of novel thin film solar cell materials using physical-vapor deposition based combinatorial synthesis

approaches and high-throughput semiconductor characterization techniques, including temporally and spatially resolved investigations of the charge carrier dynamics in these materials. Dr. Unold received a PhD in physics at the University of Oregon, and performed postdoctoral research at the National Renewable Energy Laboratory, USA, the Universität Oldenburg and at the Max-Born Institute for Nonlinear Optics, Berlin, before joining HZB.

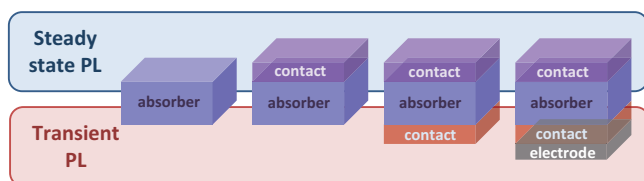


Figure 1. Overview over the different sample and photoluminescence measurement types that be applied to halide perovskite thin-films and devices. There are essentially two types of measurements, namely steady-state PL, where the absolute intensity and the spectrum provide information about the sample, and the transient PL where the shape of the transient has to be analyzed. Depending on the sample type (i.e., absorber layer on glass or absorber layer with one or two contact layers attached), the complexity of the interpretation of data increases from left to right.

avalanche photodiode (APD) or a photomultiplier tube, is used in combination with time-measuring electronics. The detection unit measures the time which passes in between the excitation laser pulse and the first photon emitted and recorded by the detection unit. Since the emission of photons is statistical, the measurement is performed at a high repetition rate (kHz–MHz) which leads to the generation of a histogram of photon emission times that resembled the luminescence decay observed for the sample. If spectral information is needed, the luminescence signal passes through a monochromator placed before the photon detection unit. The time resolution (shortest times that can be resolved) of this method is given by the autocorrelation of the laser pulse with the time-response of the detector and typically ranges from about 50 ps to several ns. Since typically high-frequency pulsed lasers (kHz–MHz) are used in these experiments, it is important to ensure that the repetition rate is smaller than the inverse PL decay time, otherwise artifacts can develop from state-filling effects. As will be discussed further below, changing the excitation conditions can strongly affect the luminescence data and can completely change the dominating recombination path. Often in literature only a measurement at one fluence is shown and the excitation conditions are not specified fully (J cm^{-2}), which sometimes precludes evaluation, interpretation, and comparison by the

reader. Thus, experimentalists are strongly advised to state the excitation flux and record and report transients as a function of excitation density. This involves measuring both the laser intensity at the sample and the spot size, which can be measured by a profiling unit or by scanning across a well-defined edge. Both the excitation spot size and the luminescence collection area are determined by the numerical aperture of the excitation and collection optics and can be adjusted to allow excitation on length scales much larger than the diffusion length in halide perovskites. For experiments using conducting layers, for example, highly doped transport layers and/or contacts or complete solar cells, partial illumination of the sample area may lead to distortions, for example, lateral currents and reduction of the luminescence intensity, as the bias voltage in the sample may be undefined. Moreover, in TRPL measurements the repetition rate of the pulsed laser system has to be adjusted such that the excited sample has enough time to return to the relaxed (dark) state, otherwise, charge carriers will accumulate in the sample which will lead to unpredictable additional recombination losses. This is particularly critical for the lead-halide perovskite samples showing very long carrier lifetimes in the microsecond range. Here, repetition rates significantly below 100 kHz should be used in order to obtain consistent data. Moreover, it is advised to check different excitation wavelengths, as for example, laser excitations using short wavelengths ($<500\text{ nm}$) will lead to a rather narrow generation profile. The diffusion of charge carriers out of this initial generation profile may lead to an initial drop in the TRPL decay and to a bi-exponential decay which often complicates the interpretation of the data. In particular, it was observed that using long wavelength excitation (700 nm) on perovskites with a gap of 1.6 eV led to a single-exponential decay behavior at low fluences.^[8]

2.2. Steady-State Photoluminescence Spectra

A typical setup for steady-state photoluminescence can be almost identical to the setup used in TRPL, but often employs a charge-coupled device (CCD) as a detector behind the

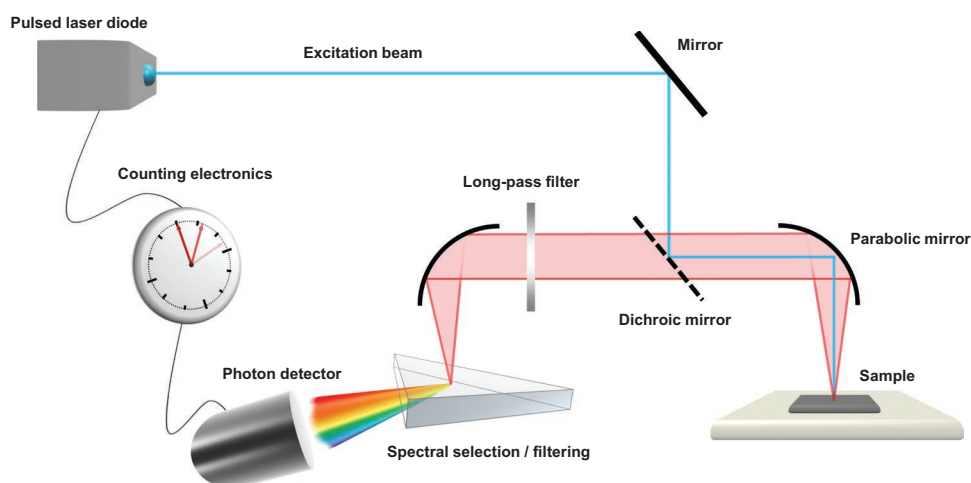


Figure 2. Setup, typically used to measure transient photoluminescence decays. The pulsed laser diode is exciting the sample, whose luminescence is directed toward a detector (e.g., a photomultiplier tube [PMT]) connected with photon counting electronics. Alternatively a lens-based system can be used, the advantage of mirrors being the elimination of chromatic aberrations.

monochromator, thus enabling to capture a full spectrum at once. The most common excitation sources used in modern instruments are solid-state laser diodes, which are available at various wavelengths and for a wide range of laser powers. Excitation and detection can be performed in a confocal arrangement or with separate beam paths.

In order to determine the PL quantum efficiency of samples, a PL setup calibrated to absolute photon numbers has to be used. In the most common implementation of this type of measurement, the sample is placed in an integrating sphere and is excited with a laser through an optical fiber which is coupled to the sphere. The intensity of the exciting laser can be adjusted to a 1 sun equivalent intensity as detailed below. A second optical fiber can be used to couple the output of the integrating sphere to a (silicon) CCD camera. The system is calibrated by shining a calibrated halogen lamp with specified spectral irradiance into the integrating sphere. A spectral correction factor must be used to match the spectral output of the detector to the calibrated spectral irradiance of the lamp. It should be noted that data are usually recorded as a function of wavelength with constant wavelength intervals using a monochromator or spectrograph. Converting the luminescence spectra, $Y_{\text{PL}}/\Delta\lambda$, to represent constant energy intervals, $Y_{\text{PL}}/\Delta E$, thus requires multiplying the recorded signal with $\Delta\lambda/\Delta E = \lambda^2/c$. A second implementation is to employ hyperspectral imaging^[16,19,33,34] in which the sample is illuminated with a homogeneous broad-beam laser or LED-source and the luminescence is recorded as a complete image with a CCD camera. Spectral resolution at each pixel can be obtained by using an appropriate spectral filtering system, either given by a band pass wheel or tunable band pass system. In this way a hyperspectral data cube containing luminescence spectra at each pixel can be obtained.

As will be discussed below the recombination properties of semiconductors (in this case halide perovskites) depend strongly on the excitation conditions used in the measurement. To make measurements comparable and allow correlation with standard testing conditions of solar cells, the (monochromatic) excitation photon flux for a given material should be matched to the excitation that would be expected by exposing the material or solar cell to sun light (AM1.5G–100 mW cm⁻²).^[35] This is shown assuming a step-like absorption onset in **Figure 3**, where also the corresponding excitation intensity for different monochromatic excitation wavelengths is shown on the right axis. For a typical methylammonium lead iodide (MAPI) perovskite with a band gap of ≈ 1.6 eV this corresponds to a photon flux of 1.6×10^{17} cm⁻² s⁻¹ and ≈ 56 mW cm⁻² illuminating with 532 nm light.

3. Basic Concepts

This tutorial aims at providing useful information for a broad readership with varying previous knowledge on the topic of photoluminescence characterization of perovskite layers and solar cells. The following section will introduce the key basic concepts required for understanding the subsequent sections. Those readers who are already familiar with concepts such as generation and recombination rates, quasi-Fermi level splittings, charge carrier lifetimes, and luminescence quantum

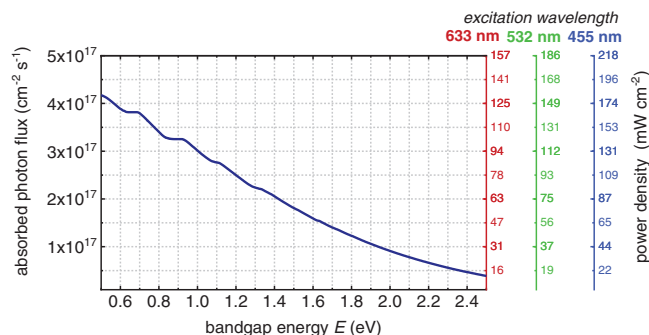


Figure 3. AM1.5G equivalent steady-state absorbed photon flux for different bandgap energies, assuming a step-function-like absorptivity where all the photons with energy above the bandgap are absorbed. The power density required to achieve such photon flux values for different excitation wavelengths is stated on the right axis.

efficiencies can skip Section 3 and directly continue with the application of the concepts to perovskite layer stacks and devices in Sections 4–6.

3.1. Generation and Recombination Rates

Photoluminescence is based on measuring the emission of photons from a semiconductor that have been created by radiative recombination. Radiative recombination requires one electron and one hole to participate in a recombination process. Once the photon is created internally by radiative recombination, it may be emitted from the sample or alternatively it may be reabsorbed by the sample itself before it is able to leave the sample. Because of the higher refractive index of the semiconductor sample relative to the air surrounding it, the fraction of photons trapped inside the sample by total internal reflection might be quite substantial and the fraction of reabsorbed photons typically strongly exceeds the fraction of emitted photons. Because light outcoupling is typically independent of the concentration of charge carriers, the photoluminescence intensity Y_{PL} emitted from the semiconductor also depends on the product np of electron and hole concentrations. In order to quantitatively understand the amount of photoluminescence emitted from a semiconductor, one therefore has to find a way of calculating the electron and hole concentrations as a function of external excitation. This can be done using the continuity equations which read for electrons

$$\frac{dn}{dt} = G_{\text{ext}}(x, t) + G_{\text{int}}(x, t, n, p) - R(x, t, n, p) + D_n \frac{d^2 n(x, t)}{dx^2} + F\mu_n \frac{dn(x, t)}{dx} \quad (1)$$

and holes

$$\frac{dp}{dt} = G_{\text{ext}}(x, t) + G_{\text{int}}(x, t, n, p) - R(x, t, n, p) + D_p \frac{d^2 p(x, t)}{dx^2} - F\mu_p \frac{dp(x, t)}{dx} \quad (2)$$

Here, x is the position normal to the cell surface, t is the time, n and p are the electron and hole concentrations, $D_{n/p} = \mu_{n/p} kT/q$ are the diffusion constants for electrons and holes, kT/q is the thermal voltage (25.8 mV at room temperature), F is the electric

field, $\mu_{n/p}$ are the mobilities, R is the recombination rate, G_{ext} is the generation rate of electron hole pairs due to external illumination (e.g., by the laser pulse in a transient experiment) and G_{int} is the internal generation rate due to the absorption of photons generated by radiative recombination within the device itself (i.e., due to photon recycling).^[36–38] The last two terms in Equations (1) and (2) are the diffusion and drift terms that determine the flow of electrons and holes. We note that these equations do not take into account the kinetics of trapping and detrapping, which may occur in case of shallow defects present in the semiconductor. To include these effects, an additional differential equation for the occupation of the trap level has to be considered as described in previous works.^[39,40] Thermal emission from shallow traps can significantly influence PL transients, in particular for materials with very short (subnanosecond) minority carrier lifetimes, since then the apparent carrier lifetime represents the detrapping time rather than the actual non-radiative recombination lifetime.^[41] However, this effect becomes less important for the much longer carrier lifetimes observed for halide perovskites. Here the use of the more complicated differential equation system with additional parameters can lead to overfitting, thus masking the essence of the physical parameters that can be extracted from the experiments reliably. Therefore in the remainder of the manuscript, we will

not consider trapping/detrapping specifically in our description of data and analysis.

In many practical situations, the continuity equations can be substantially simplified which then allows finding analytical solutions for the concentration of electrons and holes in a steady-state or a transient experiment. In the following, we will discuss a few relevant cases to show how to arrive at analytical solutions for the electron (or hole) concentrations and in **Tables 1** and **2** we present an overview over the different solutions that are frequently used in literature and give details on their applicability. In the following, we will also introduce the key criteria leading to different photoluminescence decays (under pulsed excitation) or different luminescence intensities (under steady-state excitation). These criteria are the nature of the involved recombination processes and the ratio of the electron and hole densities under excitation, that is, whether the doping density of the semiconductor sample is higher or lower than the concentration of photogenerated electrons and holes.

Analytical solutions of the continuity equation can be used if the terms for diffusion and drift currents can be neglected. This is a good approximation for semiconductor films on glass under high illumination conditions that have no contacts and therefore no built-in potential difference

Table 1. Solutions of the equation $G_{\text{ext}} = R(\Delta E_F)$ for the quasi-Fermi level splitting ΔE_F in high- and low-level injection as a function of the radiative recombination coefficient k_{rad} , the reabsorption probability p_r , and the electron and hole lifetimes τ_n and τ_p .

High level injection ($n = p$)	
Equation to solve	$G_{\text{ext}} = \left[k_{\text{rad}}(1 - p_r)n^2 + \frac{n}{(\tau_p + \tau_n)} \right]$
Solution for the quasi-Fermi level splitting	$\Delta E_F = kT \ln \left(\frac{n^2}{n_i^2} \right) = 2kT \ln \left(\frac{\sqrt{1 + 4k_{\text{rad}}(1 - p_r)(\tau_p + \tau_n)^2 G_{\text{ext}} - 1}}{2k_{\text{rad}}(1 - p_r)(\tau_p + \tau_n)n_i} \right)$
Solution in the radiative limit (i.e., SRH lifetimes are infinitely long)	$\Delta E_F = kT \ln \left(\frac{n^2}{n_i^2} \right) = kT \ln \left(\frac{G_{\text{ext}}}{(1 - p_r)k_{\text{rad}}n_i^2} \right)$
Solution for short SRH lifetimes (radiative recombination neglected)	$\Delta E_F = kT \ln \left(\frac{n^2}{n_i^2} \right) = 2kT \ln \left(\frac{G_{\text{ext}}(\tau_p + \tau_n)}{n_i} \right)$
Low level injection ($n \ll p$)	
Equation to solve	$G_{\text{ext}} = \left[k_{\text{rad}}(1 - p_r)np + \frac{n}{\tau_n} \right]; p = \text{const.}$
Solution for the quasi-Fermi level splitting	$\Delta E_F = kT \ln \left(\frac{n}{n_0} \right) = kT \ln \left(\frac{G_{\text{ext}}}{k_{\text{rad}}(1 - p_r)pn_0 + \frac{n_0}{\tau_n}} \right)$
Solution in the radiative limit (i.e., SRH lifetimes are infinitely long)	$\Delta E_F = kT \ln \left(\frac{n}{n_0} \right) = kT \ln \left(\frac{G_{\text{ext}}}{(1 - p_r)k_{\text{rad}}pn_0} \right)$
Solution for short SRH lifetimes (radiative recombination neglected)	$\Delta E_F = kT \ln \left(\frac{n}{n_0} \right) = kT \ln \left(\frac{G_{\text{ext}}\tau_n}{n_0} \right)$

The term $k_{\text{rad}}p_rnp$ corresponds to the internal generation rate G_{int} in Equations (1) and (2). In the following, we always assume that in low level injection, electrons are the minority carriers and holes are the majority carriers. The equations for high level injection are illustrated in Figure 4. Note that we neglect Auger recombination and that the situation described corresponds to one where all diffusion and drift currents can be neglected and hence the whole system can be treated in zero spatial dimensions.

Table 2. Solutions of the equation $-dn/dt = R(\Delta E_F)$ for $n(t)$ in high- and low-level injection as a function of the radiative recombination coefficient k_{rad} , the reabsorption probability p_r , and the electron and hole lifetimes τ_n and τ_p .

High level injection ($n = p$)	$Y_{PL} \propto n^2(t)$
Equation to solve	$-\frac{dn}{dt} = \left[k_{rad}(1-p_r)n^2 + \frac{n}{(\tau_p + \tau_n)} \right]$
Solution for $n(t)$	$n(t) = \frac{n(0)\exp(-t/(\tau_p + \tau_n))}{1 + n(0)k_{rad}(1-p_r)(\tau_p + \tau_n)[1 - \exp(-t/(\tau_p + \tau_n))]}$
Solution in the radiative limit (i.e., SRH lifetimes are infinitely long)	$n(t) = \frac{n(0)}{1 + n(0)k_{rad}(1-p_r)t}$
Solution for short SRH lifetimes (radiative recombination neglected)	$n(t) = n(0)\exp(-t/(\tau_p + \tau_n))$
Low level injection ($n \ll p$)	$Y_{PL} \propto n(t)$
Equation to solve	$-\frac{dn}{dt} = \left[k_{rad}(1-p_r)np + \frac{n}{\tau_n} \right]; p = const.$
Solution for $n(t)$	$n(t) = n(0)\exp(-t/([k_{rad}(1-p_r)p]^{-1} + \tau_n))$
Solution in the radiative limit (i.e., SRH lifetimes are infinitely long)	$n(t) = n(0)\exp(-t[k_{rad}(1-p_r)p])$
Solution for short SRH lifetimes (radiative recombination neglected)	$n(t) = n(0)\exp(-t/\tau_n)$

We always assume that in low level injection, electrons are the minority carriers and holes are the majority carriers. The equations for high-level injection are illustrated in Figure 5. Note that we neglect Auger recombination and that the situation described corresponds to one where all diffusion and drift currents can be neglected and hence the whole system can be treated in zero spatial dimensions.

between contacts. The high illumination conditions typically encountered during PL measurements will ensure that surface band bending as observed, for example, in surface photovoltage measurements is minimized.^[42] Hence, if we consider for simplicity a system with no spatial gradients of electron or hole concentrations or the electrostatic potential, the continuity equations simplify substantially. If we further assume that the doping density is negligible small relative to the photogenerated carrier density (a situation called high level injection), we may write

$$\frac{d\Delta n}{dt} = \frac{d\Delta p}{dt} = G_{ext}(t) + G_{int}(t, n) - R(t, n) \quad (3)$$

where $\Delta n = n - n_0$ is the excess electron concentration relative to the equilibrium concentration n_0 and Δp is the excess hole concentration. Note that n_0 or p_0 would include the doping densities if the sample is doped. In steady-state, $d\Delta n/dt = 0$, and the continuity equation yields

$$G_{ext} + G_{int}(n) = R(n) \quad (4)$$

From this balance equation, we obtain a steady-state concentration of electrons and holes if we know how the recombination rate depends on charge-carrier density. We also know that the luminescence emission flux Y_{PL} is proportional to the product of electron and hole concentrations (if the semiconductor is intrinsic they are equal), that is, $Y_{PL} \propto n^2$. The photoluminescence flux therefore allows us to calculate the quasi-Fermi level splitting ΔE_F in the absorber layer by using

$$\Delta E_F = kT \ln \left(\frac{n^2}{n_i^2} \right) \quad (5)$$

Thus, we conclude that the absolute intensity of steady-state photoluminescence measures the quasi-Fermi level splitting of the luminescing material. This quasi-Fermi level splitting will depend on the illumination conditions (contained in G_{ext}), the Shockley-Read-Hall (SRH) lifetime, the prefactor of recombination (in this example the radiative recombination coefficient k_{rad}) and on the equilibrium concentration of charge carriers n_i with the latter containing the effective density of states N_C and N_V (for conduction and valence band) and the band gap E_g via $n_i^2 = N_C N_V \exp(-E_g/kT)$. The presence of n_i in Equation (5) ensures that for a given generation and recombination rate, higher band gap materials (i.e., materials with lower n_i) tend to have a higher quasi-Fermi level splitting. Note that in the often encountered case, where the luminescence is only known in relative units (i.e., sample A luminesces twice as strongly as sample B), absolute differences in the quasi-Fermi level between the two samples can be obtained (the quasi-Fermi level splitting in sample A is higher by $kT \times \ln(2) \approx 18$ meV if n_i doesn't change) but the absolute value would be unknown. This is due to the fact that quasi-Fermi level splitting depends logarithmically on the luminescence intensity. Hence, unknown multiplicative factors in the luminescence become unknown additive offsets in the quasi-Fermi level splitting.

The importance of the purely optical measurement of the quasi-Fermi level splitting by photoluminescence lies in the possibility to measure the upper limit of the open-circuit voltage that a certain layer or layer stack would be able to provide if contacts are attached that do not lead to additional recombination losses.^[8,9,13,15,16,19,33] Figure 4 shows how the quasi-Fermi level splitting depends on the SRH lifetime $\tau = \tau_p + \tau_n$. For lower lifetimes, ΔE_F scales with $\ln(\tau)$ while it approaches a constant

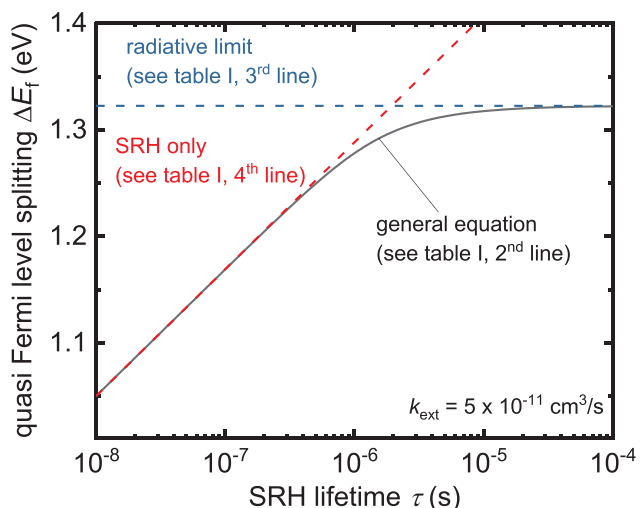


Figure 4. Simulation showing the relation between the quasi-Fermi level splitting of a spatially homogeneous semiconductor layer in high level injection ($n = p$) with the intrinsic carrier concentration of MAPb ($n_i = 8 \times 10^4 \text{ cm}^{-3}$) and using a typical value of $k_{\text{ext}} = k_{\text{rad}}(1 - p_r)$. For high values of the SRH lifetime $\tau = \tau_p + \tau_n$, the quasi-Fermi level splitting approaches the radiative limit given by $\Delta E_F = kT \ln(G_{\text{ext}} / [(1 - p_r)k_{\text{rad}}n_i^2])$ (dashed blue line). For lower values, the quasi Fermi level splitting increases linearly with the logarithm of the lifetime (dashed red line). The equations governing the complete behavior (solid black line) and the limiting situations (red and blue) are given in Table 1. The generation rate used is $G_{\text{ext}} = 5.3 \times 10^{21} \text{ cm}^{-3} \text{ s}^{-1}$ which would be a typical generation rate for a thin perovskite film, assuming an AM1.5G equivalent photon flux of $\Phi = 1.6 \times 10^{17} \text{ cm}^{-2} \text{ s}^{-1}$, an absorber thickness $d = 300 \text{ nm}$, and using $G_{\text{ext}} = \Phi/d$.

value for high lifetimes. This constant value is the radiative limit given by $\Delta E_F = kT \ln(G_{\text{ext}}/k_{\text{ext}}n_i^2)$ (see Table 1).

3.2. Charge Carrier Lifetimes

3.2.1. Doped Semiconductors, Low Level Injection

Most classical semiconductor materials are doped when used in optoelectronic devices. If the doping is high enough, the majority carrier density will be higher than the minority carrier density even under moderate illumination conditions. This case is called low level injection and it leads to the convenient situation that all recombination mechanisms become linear in minority carrier density. The three classical recombination mechanisms that are typically considered in semiconductors are Auger recombination, radiative recombination, and defect assisted recombination, which can be described by the Shockley–Read–Hall recombination rate.^[43,44] Table 3 provides the equations for these recombination mechanisms in different scenarios (the general equations, the equations for high level and those for low level injection).

Taking the general equations, one can express the total recombination rate R_{tot} in terms of the charge carrier density as

$$R_{\text{tot}} = \left[k_{\text{rad}}(1 - p_r) + \frac{1}{n\tau_p + p\tau_n} + C_n n + C_p p \right] (np - n_i^2) \quad (6)$$

where the first term is the effective rate of radiative recombination as introduced above. Here the radiative recombination rate $k_{\text{rad}}np$

is slowed down by the internal generation rate $G_{\text{int}} = k_{\text{rad}}p_r np$. The second term represents Shockley-Read-Hall recombination via a deep defect with electron and hole lifetimes τ_n and τ_p and the last two terms represent Auger recombination with Auger coefficients C_n and C_p . In low level injection in a p-type semiconductor with doping density N_A , Equation (6) will simplify to

$$R_{\text{tot}} = \left[k_{\text{rad}}(1 - p_r)N_A + \frac{1}{\tau_n} + C_p N_A^2 \right] (n - n_0) =: \frac{\Delta n}{\tau_{\text{eff}}} \quad (7)$$

where $n_0 = n_i^2/N_A$ is the equilibrium concentration of electrons in the p-type semiconductor with a density N_A of ionized acceptor atoms which leads to an equilibrium hole density $p_0 = N_A$. Equation (7) implies that the dynamics of recombination can be summed up in an effective lifetime τ_{eff} that is the inverse of the term in the square brackets. The significance of the lifetime is that it can be measured in a transient experiment that is sensitive to the charge-carrier concentration such as transient photoluminescence. If we excite the doped semiconductor with a laser pulse, the decay of charge carriers follows the differential equation $-dn/dt = (n - n_0)/\tau_{\text{eff}}$ with the solution $\Delta n(t) = \Delta n(t = 0)\exp(-t/\tau_{\text{eff}})$. Given that in a doped semiconductor, the luminescence is proportional to the minority carrier density n , the decay constant gives the effective lifetime that can then be interpreted in terms of the different possible recombination mechanisms discussed above. While the (effective) lifetime is easy to determine, the discrimination between the recombination mechanisms is only possible if the excitation conditions are varied to go from low to high level injection or if additional information is present (e.g., about the magnitude of the Auger coefficients and radiative recombination coefficients).

3.2.2. Intrinsic Semiconductors, High Level Injection

Lead-halide perovskites typically behave as intrinsic or low doped semiconductors in photoluminescence experiments. In addition, lead-halide perovskites have sharp absorption onsets that lead to values for the radiative recombination coefficient k_{rad} that are similar to that of typical direct semiconductors such as GaAs.^[45–48] We will later show (see Figure 6a) that the Auger coefficients are essentially irrelevant at the illumination conditions present in solar cells under normal, unconcentrated operation, which is an advantage over silicon solar cells.^[49] Hence, in order to describe steady-state photoluminescence analytically, one has to solve the quadratic equation

$$G_{\text{ext}} = \left[k_{\text{ext}}n^2 + \frac{n}{(\tau_p + \tau_n)} \right] \quad (8)$$

for the carrier concentration n . Note, that the term $k_{\text{ext}} = k_{\text{rad}}(1 - p_r)$ denotes the externally observed radiative constant, which is obtained from the analysis of photoluminescence transients. From the carrier concentration, the quasi-Fermi level splitting follows in high level injection via $\Delta E_F = kT \ln(n^2/n_i^2)$, which results in the expressions given in Table 1. Table 1 shows the analytical solutions for the quasi-Fermi level splitting and various simplifications of the general equation for situations in

Table 3. Equations for the recombination rates in different scenarios (high level injection and low-level injection).

General equations ^{a)}	
Radiative recombination rate	$R_{\text{rad}} = [k_{\text{rad}}(1 - p_r)] (np - n_i^2)$
SRH recombination rate	$R_{\text{SRH}} = \frac{(np - n_i^2)}{(n + n_1)\tau_p + (p + p_1)\tau_n}$
SRH recombination rate for a deep defect	$R_{\text{SRH}} = \frac{(np - n_i^2)}{n\tau_p + p\tau_n}$
Auger recombination rate	$R_{\text{Aug}} = [C_n n + C_p p] (np - n_i^2)$
High level injection ($n = p$)	
Radiative recombination rate	$R_{\text{rad}} = [k_{\text{rad}}(1 - p_r)] (n^2 - n_i^2)$
SRH recombination rate	$R_{\text{SRH}} = \frac{(n^2 - n_i^2)}{(n + n_1 + p_1)(\tau_p + \tau_n)}$
SRH recombination rate for a deep defect (and $np > n_i^2$)	$R_{\text{SRH}} = \frac{n}{\tau_p + \tau_n}$
Auger recombination rate	$R_{\text{Aug}} = [C_n + C_p] n^3$
Low level injection ($n \ll p, p = N_A$)	
Radiative recombination rate	$R_{\text{rad}} = [k_{\text{rad}}(1 - p_r)] (nN_A - n_i^2) \propto n$
SRH recombination rate	$R_{\text{SRH}} = \frac{(nN_A - n_i^2)}{(N_A + p_1 + n_1)\tau_n} \propto n$
SRH recombination rate for a deep defect (and $np > n_i^2$)	$R_{\text{SRH}} = \frac{\Delta n}{\tau_n} \propto n$
Auger recombination rate	$R_{\text{Aug}} = C_p N_A (nN_A - n_i^2) \propto n$

^{a)}We stress here that the common assignment of SRH, radiative and Auger recombination, respectively, to first order, second order, and third order processes in electron concentration n , only works in high level injection. In low level injection, all three mechanisms are linear in n . In the context of SRH recombination, we use the abbreviations $n_1 = N_C \exp[(E_T - E_C)/kT]$ and $p_1 = N_V \exp[(E_V - E_T)/kT]$, where E_C is the conduction band edge, E_V is the valence band edge, and E_T is the trap level.

which either radiative or SRH recombination dominate and for high and low-level injection.

In case of a transient photoluminescence experiment, the electron and hole concentrations decay after a laser pulse has excited charge carriers. For times Δt after the laser pulse, the differential equation to solve is

$$-\frac{dn}{dt} = \left[k_{\text{rad}}(1 - p_r)n^2 + \frac{n}{(\tau_p + \tau_n)} \right] \quad (9)$$

which has the solutions shown in Table 2. Note that in high-level injection, the decay is faster at shorter times and higher excitation conditions, because the quadratic dependence of radiative recombination on n is dominant. At later times and/or lower excitation conditions, the exponential decay caused by SRH recombination ($R_{\text{SRH}} \propto \Delta n$) dominates the decay.

Figure 5 illustrates how typical PL transients should look like based on the equations in Table 2. Figure 5 shows PL decays normalized to the value at time $t = 0$ for three different laser fluences that lead to different carrier concentrations

($\Delta n(0) = 10^{16}$, 10^{17} , and 10^{18} cm^{-3}) at early times. The solid lines show the decay assuming a combination of radiative recombination with $k_{\text{ext}} = k_{\text{rad}}(1 - p_r) = 5 \times 10^{-11} \text{ cm}^3 \text{ s}^{-1}$ and SRH recombination with a lifetime $\tau_{\text{SRH}} = \tau_n + \tau_p = 500 \text{ ns}$. The dotted lines show the decay for radiative recombination only to illustrate which parts of the curve are caused by which of the two recombination mechanisms. At early times, radiative recombination is dominant, leading to an initial fast decay (seen in solid and dotted lines) followed by a slow decay at later times (seen only in the dotted lines). For the simulations including SRH recombination, the decay at later times is monoexponential with the slope given by the SRH lifetime $\tau_{\text{SRH}} = 500 \text{ ns}$. We note that the decays at different initial carrier concentrations differ from each other at early times, where radiative recombination dominates. At later times, the decays are parallel because SRH recombination dominates, which is linear in carrier density and hence the decay approaches $Y_{\text{PL}}(t) \propto n^2 \propto \exp(-2t/\tau_{\text{SRH}})$. This means that in this case the SRH lifetime is obtained by multiplying the decay time by a factor of 2.

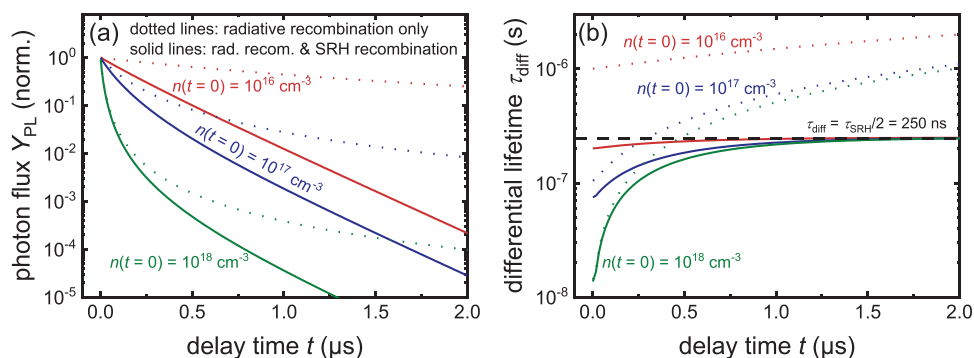


Figure 5. a) Simulation of transient photoluminescence decays of perovskite films on glass following the equations presented in Table 2 for high level injection. b) Differential lifetimes obtained from the decays shown in (a). As done in Table 2, Auger recombination is neglected. The transients are all normalized to their value at $t = 0$ (when the pulse hits the sample) and differ by the initial carrier concentration $n(0)$ set by the intensity of the pulse. The solid lines show calculations assuming radiative and SRH recombination are present ($\tau_{\text{SRH}} = 500$ ns) and the dotted lines show the situation when only radiative recombination is present. The higher the initial carrier concentration, the stronger the fast decay at short times that is indicative of higher order recombination (in this case, radiative recombination). All three solid lines, however, are parallel at later times, when the 500 ns SRH lifetime controls the monoexponential part of the decay. Note, the SRH lifetime is obtained by multiplying the (apparent) differential lifetime in panel b) by a factor 2.

Figure 5b shows the differential lifetimes $\tau_{\text{diff}}(t) = -(\ln(Y_{\text{PL}}(t)/dt))^{-1}$ obtained from taking the derivative of the logarithm of the PL intensity at every point t . For the simulations with combined SRH and radiative recombination, the differential lifetime increases for early times until it reaches a fixed value at longer times (in this example at 250 ns, that is, at $\tau_{\text{SRH}}/2$). The continuous increase at early times is due to the effect of radiative recombination which leads to a constantly changing differential lifetime. For the case of radiative recombination only (dotted lines), the differential lifetime does not saturate but continuously increases.

3.3. Origin of the Recombination Coefficients

3.3.1. Radiative Coefficient

As we have seen earlier, there are three key parameters (k_{rad} , τ_n , and τ_p) that affect both the steady-state recombination dynamics and the photoluminescence decay. Of these three parameters,

k_{rad} is the most straightforward to relate to other material properties. Radiative recombination is the inverse process of absorption of photons and subsequent creation of electron-hole pairs. Microscopic processes have to obey the principle of detailed balance,^[50] that is, the rate of radiative recombination in thermal equilibrium must equal the equilibrium rate of photogeneration. Equating the two rates (recombination on the left and generation on the right) leads to the so-called van Roosbroeck–Shockley equation.^[51]

$$k_{\text{rad}} n_i^2 = \int_0^\infty 4 \alpha n_r^2 \phi_{\text{bb}} dE \quad (10)$$

where α is the absorption coefficient, n_r is the refractive index and

$$\phi_{\text{bb}}(E) = \frac{2\pi E^2}{h^3 c^2} \frac{1}{[\exp(E/kT) - 1]} \approx \frac{2\pi E^2}{h^3 c^2} \exp\left(\frac{-E}{kT}\right) \quad (11)$$

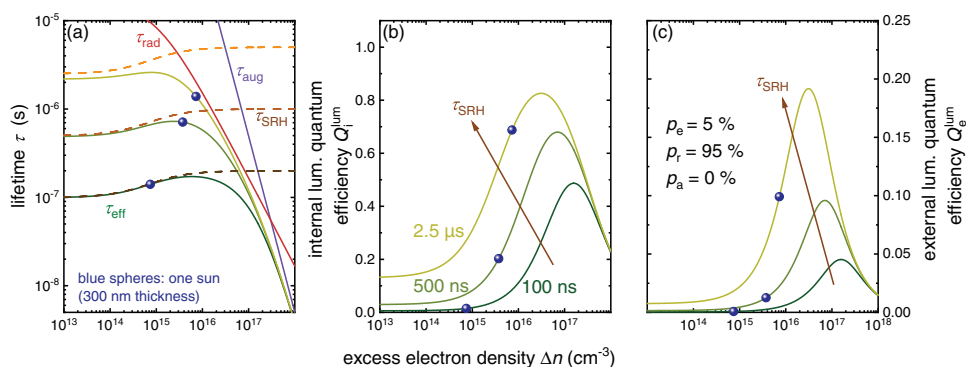


Figure 6. Simulation showing a) the combination of different contributions to the effective lifetime τ_{eff} , b) the resulting internal luminescence quantum efficiencies, and c) the external luminescence quantum efficiencies. The data are plotted for three different values of the electron and hole lifetimes, namely $\tau_p = \tau_n = 100$ ns, 500 ns, and 2.5 μs . In addition, we assume a p-type doping density $N_A = 10^{15}$ cm^{-3} to show the effect of the transition from low- to high-level injection. The used values for radiative and Auger recombination are $k_{\text{rad}} = 6 \times 10^{-11}$ $\text{cm}^3 \text{s}^{-1}$ and $C_{\text{Aug}} = 10^{-28}$ $\text{cm}^6 \text{s}^{-1}$. We note first that Auger recombination has only an effect on the effective lifetime at electron densities beyond one sun conditions (blue spheres). We also observe that lifetimes = 2.5 μs already allows achieving $Q_i^{\text{lum}} \approx 0.7$ at AM1.5G equivalent excitation, but due to the typically quite low outcoupling efficiencies, the external luminescence quantum efficiencies are substantially smaller ($\approx 10\%$) even though we assume here zero parasitic absorption.

Table 4. Recombination coefficients as reported in literature including the assumptions for the probability of parasitic absorption, for emission, and for reabsorption in the perovskite layer (in addition, we note the reported fraction X_{non} of non-radiative bimolecular recombination to the total bimolecular recombination).

Reference	k_{ext} [cm ³ s ⁻¹]	k_{rad} [cm ³ s ⁻¹]	k_{non} [cm ³ s ⁻¹]	p_a [%]	p_e [%]	p_r [%]	X_{non} [%]
Staub et al. ^[24] CH ₃ NH ₃ PbI ₃	4.8×10^{-11}	8.7×10^{-10}	0	0.0	5.5	94.5	0
Crothers et al. ^[64] CH ₃ NH ₃ PbI ₃	1.4×10^{-10} to 2×10^{-11}	6.8×10^{-10}	Neglected			79–97	0
Richter et al. ^[52] CH ₃ NH ₃ PbI ₃	8.1×10^{-11}	7.1×10^{-11}	7.2×10^{-11}	0.0	12.7	87.3	50
Richter et al. ^[52] CH ₃ NH ₃ PbI _{3-\rightarrow} Cl _x	7.9×10^{-11}	1.8×10^{-10}	5.6×10^{-11}	0.0	12.7	87.3	24
Staub et al. ^[53] CH ₃ NH ₃ PbI ₃ on 200 nm SiO ₂ /Si wafer	4.6×10^{-11}	5.9×10^{-11}	3.1×10^{-11}	17.0	9.0	74.0	34
Braly et al. ^[65] CH ₃ NH ₃ PbI ₃	1.4×10^{-11}	2.3×10^{-10}	0	0.0	6.1	93.9	0
Zhang et al. ^[66] (DFT) CH ₃ NH ₃ PbI ₃		1.1×10^{-10} to 6×10^{-11}					

is, the spectrum of a planar black body with temperature T emitting into a hemisphere. The van Roosbroeck–Shockley equation can be used to determine the radiative recombination coefficient k_{rad} if the absorption coefficient and n_i^2 are known.^[24] Note that this value of k_{rad} will be different from the recombination coefficient that follows from transient photoluminescence decay, because the latter would measure $k_{\text{ext}} = k_{\text{rad}}(1 - p_r)$. Comparing the recombination coefficients obtained from steady-state absorption and from transient methods, therefore requires a good estimate of the reabsorption probability p_r .

An overview of literature data for direct recombination coefficients are presented in Table 4. Surveying the literature reveals that the derived external radiative recombination constant, which includes photon-recycling, varies considerably within a factor of 10 for thin film thicknesses of around 400 nm. Interestingly, also k_{rad} , which is an intrinsic property of the material, varies more than one order of magnitude between different studies. This highlights the difficulty in precisely estimating such an important parameter. If parasitic absorption is neglected, then the differences in k_{ext} would be solely due to different escape probabilities of photons for the samples measured in the different studies, which will be discussed further below. There are also some reports in the literature, where it was only possible to explain or model experimental data if a non-radiative quadratic recombination coefficient k_{non} was introduced.^[52,53] For these cases, we also include the value for k_{non} and the fraction $X_{\text{non}} = k_{\text{non}}/(k_{\text{non}} + k_{\text{rad}})$ in Table 4. There is currently no generally accepted explanation for this observation. Non-radiative band-to-band transitions could in principle proceed via multiphonon processes as for defect assisted recombination. However, one would expect the transition rates to be negligibly small, especially for materials with low phonon energies.^[54,55] Auger recombination involving two free and one trapped carrier could also be $\approx np$, while being non-radiative in nature as suggested by Richter et al.^[52] However, in the presence of defects one would not expect Auger processes to be dominant relative to multiphonon-assisted SRH recombination.^[56,57] Therefore,

the jury is still out on the existence, nature, and importance of non-radiative band to band recombination in halide perovskites. We therefore proceed discussing the situation, where band-to-band recombination is entirely radiative and SRH recombination is the dominant non-radiative recombination mechanism.

3.3.2. Shockley–Read–Hall Lifetimes

Understanding the lifetimes τ_n and τ_p for non-radiative SRH recombination is somewhat more difficult. In the classical interpretation of the SRH lifetimes as being due to recombination via one dominant defect level, the lifetimes depend inversely on the density of said defect and inversely on a kinetic prefactor that we could call the capture coefficient for electrons or holes of that defect. These capture coefficients are usually thought to be determined by the efficiency of multiphonon transitions between a band state and the defect state.^[58–61] These multiphonon transitions become faster if electron-phonon coupling is strong and if the energy of the transition is small in units of the phonon energy. In addition, Coulomb attraction accelerates the kinetics of recombination depending on the materials permittivity and effective mass.^[55] A detailed description of the origin of the recombination coefficient goes beyond the scope of the present tutorial and we refer the interested reader to a series of book chapters and review articles on the topic.^[54,61–63]

3.4. Defect Tolerance

Because of the necessity to allow efficient light absorption in solar cell materials and because of detailed balance between absorption and emission (see Equation (10)), radiative recombination is an unavoidable process. However, recombination can lead to losses relative to the Shockley–Queisser model^[67] of solar cells if non-radiative processes occur.^[68–70] In perovskites, these non-radiative processes occur mainly via defect assisted

recombination that may occur in the bulk, at grain boundaries or at surfaces and interfaces to other layers.^[71,72] Non-radiative phonon-assisted processes become less likely if the energetic transitions get larger.^[54,58–61] Hence the presence of localized states in the band gap will accelerate non-radiative transitions, because it reduces the energy difference between individual electronic states that electrons have to overcome during a phonon-assisted recombination process. Whether a defect will be highly recombination active depends on its properties and most importantly on its distance from the two band edges (conduction and valence band). Shallow defects are more likely to trap either electrons or holes while deeper defects are likely to trap both types of carriers and thereby accelerate recombination.

Relative to other semiconductors, perovskites such as MAPI (CH₃NH₃PbI₃) feature very long SRH lifetimes often derived from photoluminescence decays, which suggests that defects do less harm than in many other inorganic semiconductors.^[73–75] This observation has been frequently described as defect tolerance^[74,76,77] and a variety of explanations have been put forward.^[72] These include in particular the antibonding valence band maxima of MAPI which leads to the situation that most intrinsic point defects are shallow defects^[78] and thereby may not be able to capture either of the two charge carrier types efficiently. Another possibility is that defect densities are generally lower than in most other polycrystalline materials.^[79] A third possible explanation could be that the capture cross sections are lower than in other semiconductors, which for a given concentration of defects would also lead to longer lifetimes.^[54] Future work will have to show which of the three aspects is decisive to explain the long lifetimes in lead-halide perovskites and whether these features can also be found in other so far not explored semiconductor families.

3.5. Luminescence Quantum Efficiencies

Radiative recombination is a necessary requirement for any photovoltaic device, because it is the inverse process of absorption.^[51] Since high absorption coefficients are a prerequisite for efficient photocurrent generation in solar cells, the figure of merit for recombination is not necessarily a measured long lifetime but the ratio of the radiative to the total recombination rate.^[68,70,80,81] This ratio is called the internal luminescence quantum efficiency.

$$Q_i^{\text{lum}} = \frac{R_{\text{rad}}}{R_{\text{rad}} + R_{\text{nrad}}} = \frac{k_{\text{rad}} np}{k_{\text{rad}} np + R_{\text{SRH}} + R_{\text{Aug}}} \quad (12)$$

The internal luminescence quantum efficiency cannot directly be measured in a steady-state luminescence experiment. This is due to the fact that the photons created with the rate R_{rad} by radiative recombination in the semiconductor volume are not necessarily emitted into the hemisphere above (and/or below the semiconductor layer). In general, one part of the photons created in the volume will be emitted with probability p_e , some will be reabsorbed in the absorber layer itself with probability p_r and some might be reabsorbed in additional layers of the sample stack (with probability p_a).^[82] Parasitic absorption will not be a substantial problem in case of

luminescence experiments on films on glass, while the effect will likely be substantial in case of luminescence experiments on full devices that contain several carrier transport layers and electrodes that feature neither perfect transmission nor perfectly reflection. Later, in Section 4, we will discuss in more detail how to calculate p_e (see Equation (17)) and how changes in p_a can affect the experimental data (see Section 4.4).

A quantity that is directly accessible by experiment is the external luminescence quantum efficiency, which is defined as the ratio of fluxes or current densities. We may write

$$Q_e^{\text{lum}} = \frac{Y_{\text{em}}}{Y_{\text{rec}}} = \frac{p_e R_{\text{rad}}}{R_{\text{nrad}} + (1 - p_r) R_{\text{rad}}} = \frac{p_e Q_i^{\text{lum}}}{1 - p_r Q_i^{\text{lum}}} \quad (13)$$

where Y_{em} is the emitted photon flux and Y_{rec} is the recombination flux (of particles not of charge), that is, the spatial integral over the total recombination rate (radiative and non-radiative).

If we neglect Auger recombination and approximate the SRH recombination by $\Delta n / \tau$, where τ is the limiting lifetime (τ_n or τ_p in low injection, $\tau_n + \tau_p$ in high injection), then the external quantum efficiency can be written as

$$Q_e^{\text{lum}} = \frac{p_e k_{\text{rad}} np}{\frac{\Delta n}{\tau} + (p_e + p_a) k_{\text{rad}} np} \quad (14)$$

where $p = \Delta p + N_A$ in the general case, and $n = p$ applies for high level injection conditions $\Delta n, \Delta p \gg N_A$. The equation shows that assumptions about p_e, k_{rad}, N_A are necessary in order to correlate Q_e^{lum} with the carrier lifetime, which will be further discussed below.

Figure 6 presents simulations illustrating the relation between charge carrier lifetimes in panel a) to internal luminescence quantum efficiencies in panel b) and finally to external luminescence quantum efficiencies in panel c). All three quantities are presented as a function of excess electron density Δn and we assumed a p-type doping density $N_A = 10^{15} \text{ cm}^{-3}$ to illustrate the effect of doping on the relationships. Figure 6a shows how the three recombination mechanisms, SRH-, radiative-, and Auger-recombination affect the lifetime using fixed values for the radiative and Auger recombination coefficients and three different SRH lifetimes ($\tau_p = \tau_n = 100 \text{ ns}, 500 \text{ ns}, \text{ and } 2.5 \mu\text{s}$). The lower the excess electron density Δn , the more likely it is that a lower-order recombination mechanism dominates the lifetime. In the example chosen here, the effective lifetime is dominated by SRH recombination for the lower of the two SRH lifetimes chosen (100 and 500 ns). If we assume a SRH lifetime of 2.5 μs , however, the lifetime is already dominated by the radiative lifetime $\tau_{\text{rad}} = (k_{\text{ext}} N_A)^{-1}$. Toward higher excess electron densities Δn , radiative recombination dominates in all cases and leads to a reduction of the effective lifetime which approaches $\tau_{\text{eff}} \approx \tau_{\text{rad}} = (k_{\text{ext}} \Delta n)^{-1}$. Auger recombination is only relevant for the excess electron densities higher than one sun. The impact of the doping concentration is mainly that it sets a constant value for the radiative lifetime at low Δn and that it leads to a transition from low- to high-level injection, that is from $\tau_{\text{SRH}} = \tau_n$ for $\Delta n \ll N_A$ to $\tau_{\text{SRH}} = \tau_n + \tau_p$ for $\Delta n \gg N_A$.

Figure 6b shows the resulting internal luminescence quantum efficiency which shows a peak for each of the three SRH lifetimes. This peak at intermediate excess electron

densities Δn results from the transition from low- to high-level injection (from τ_n to $\tau_n + \tau_p$) combined with the additional losses due to Auger recombination at high fluences. The final transition to the external luminescence quantum efficiency in Figure 6c requires us to assume probabilities for photon emission, reabsorption, and parasitic absorption. We use $p_e = 5\%$ and assume that there is no parasitic absorption. This then leads to the three lines shown in Figure 6c. The peak values for Q_c^{lum} are $\approx 20\%$ for the $2.5 \mu\text{s}$ SRH lifetime that however is reduced quite drastically toward lower values of Δn .

4. Films on Glass

The simplest conceivable device geometry is the one of a perovskite film on glass. Because the interface between perovskite layers and glass substrates is typically quite inert and not particularly recombination active,^[24,83] recombination is most likely to occur at the interface to the ambient. There are different methods of passivating that interface, either by using organic passivation layers^[65,84,85] or simply by exposure to a certain amount of oxygen.^[86] If the passivation was successful, these types of layer structures feature the highest luminescence quantum efficiencies of all samples^[8,19,33,65] and can have very long photoluminescence lifetimes.^[84] In the following, we will briefly review luminescence experiments that can be done on perovskite films on glass and what information can be obtained from these measurements.

4.1. Photoluminescence Spectra

The PL spectrum of typical semiconductors will closely follow the relation.^[87]

$$Y_{\text{PL}}(E) = a(E) \phi_{\text{bb}}(E) \cdot \exp\left[\Delta E_{\text{F}} / (k_{\text{B}} T)\right] \quad (15)$$

which links the absorptance $a(E)$ (or absorptivity) of a semiconductor to its luminescence spectrum $Y_{\text{PL}}(E)$. Equation (15) is a generalization of Kirchhoff's law for thermal emission that states that the absorptance and emissivity of a body are identical. Wülfel generalized^[87–89] this law to non-thermal emission in semiconductors, that is, to luminescence. The key assumption of this generalization is that the emission originates from the recombination of free electrons and holes, whose occupation probability can be described by Fermi-Dirac statistics. Equation (15) features a spatially independent value of the quasi-Fermi level splitting. This condition of a spatially independent quasi-Fermi level splitting is never perfectly true; however, in reality it is a good approximation for thin films of lead-halide perovskites but not for mm thick crystals. Given that the absorptance $a(E) = (1 - R)(1 - \exp(-\alpha d))$ of a semiconductor increases steeply around the band gap for typical direct gap absorption coefficients, α , and then approaches a constant value, the PL spectrum of a semiconductor will be determined on the low energy side by the absorption edge and on the high energy side by the Boltzmann tail of the Bose–Einstein distribution that is part of ϕ_{bb} .

Figure 7 shows a photoluminescence spectrum and the corresponding absorption coefficient of a MAPI film on glass, which has been measured by photothermal deflection spectroscopy

(PDS) on the high energy side, and overlaid with the absorption coefficient obtained from Equation (15) on the low energy side. Together with the refractive index n , this allows to determine $k_{\text{rad}} n_i^2 = 5 \text{ cm}^{-3} \text{ s}^{-1}$ using Equation (10). Thus, if either k_{rad} or n_i^2 is known, one can determine the respective other parameter. In MAPI, the effective masses of electrons and holes are known^[90,91] to be in the range of 0.1–0.4 m_e , which gives a range of the combined effective densities of states from $N_c \times N_v = 6.2 \times 10^{35}$ to $4.0 \times 10^{37} \text{ cm}^{-6}$ using

$$N_c N_v = 2 \left(\frac{2\pi m_e kT}{h^2} \right)^{3/2} 2 \left(\frac{2\pi m_h kT}{h^2} \right)^{3/2} \quad (16)$$

With a band gap $E_g = 1.6 \text{ eV}$ this lead to a range of values for n_i of 2.7×10^4 to $2.1 \times 10^5 \text{ cm}^{-3}$ and hence k_{rad} in the case of the above data ends up in the range 70×10^{-9} to $1.1 \times 10^{-10} \text{ cm}^3 \text{ s}^{-1}$. If the photoluminescence setup is calibrated quantitatively, giving the exact number of photons emitted from the sample), the quasi-Fermi level splitting of the sample can be estimated from Equation (15) by either plugging in the measured absorptivity, or by assuming an absorptivity of $a(E) = 1$ for energies sufficiently above the band gap. This allows to directly calculate the quasi-Fermi level splitting from the y-axis intercept of the extrapolation of the high energy slope of the PL spectrum as shown in Figure 7.^[92]

4.2. Bulk Recombination

In addition to a spectral analysis of the above film on glass, we can also measure the PL decay as a function of time after a laser pulse. Figure 8 shows the decays for three different laser fluences normalized to the peak luminescence at early times (at the end of the laser pulse). We note that the decays change shape as a function of laser fluence, which suggests that both radiative and SRH recombination affect the decay. The higher

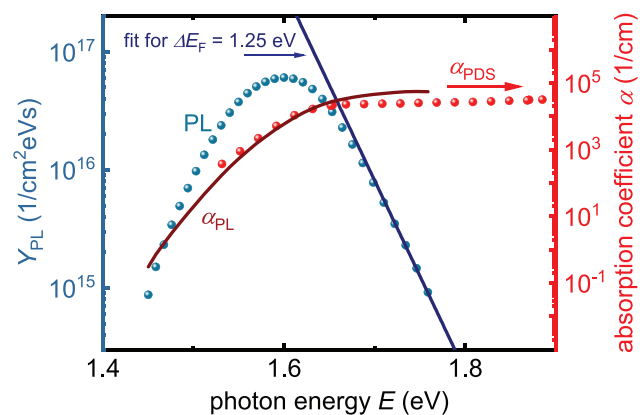


Figure 7. Absolute photoluminescence spectrum of a MAPI thin film (blue spheres, left y-axis) measured under equivalent one-sun conditions. The blue line represents the exponentially decaying part of the spectrum on the high energy side for a temperature of 300 K and $a(E) = 1$ yielding a quasi-Fermi level splitting of $\Delta E_{\text{F}} \approx 1.25 \text{ eV}$. Absorption coefficients (red lines and spheres, right y-axis) as obtained by photothermal deflection spectroscopy (α_{PDS}) as well as extracted from the photoluminescence spectrum (α_{PL}) by applying the generalized Planck radiation law.

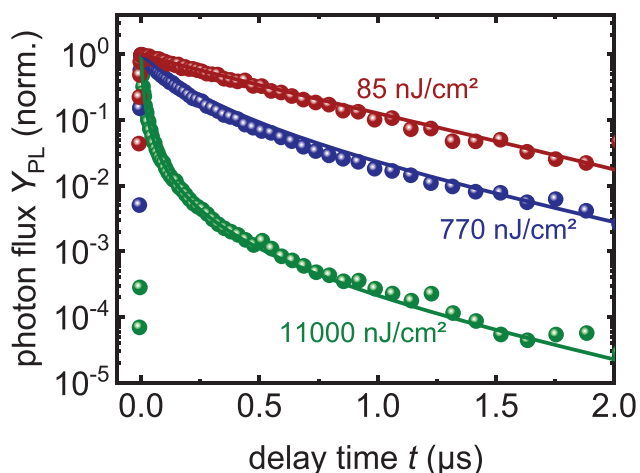


Figure 8. Normalized PL decays of a MAPI film on glass (thickness $d \approx 311$ nm) measured under different fluences. For the excitation wavelength of 496 nm this corresponds to initial carrier excitation densities of $\Delta n(0) = 7 \times 10^{15}$, 6.4×10^{16} , and 9×10^{17} cm^{-3} . Note that the higher the fluence the faster the initial decay, that is due to higher order recombination (radiative and Auger). The global fit of the data (including Auger recombination) gives $k_{\text{ext}} = (4.78 \pm 0.43) \times 10^{-11} \text{cm}^3 \text{s}^{-1}$, $C_{\text{Aug}} = C_n + C_p = (8.83 \pm 1.57) \times 10^{-29} \text{cm}^6 \text{s}^{-1}$, $\tau_n = 511 \pm 80$ ns, and $\tau_p = 871 \pm 251$ ns. Reproduced with permission.^[94] Copyright 2016, The American Physical Society.

laser fluences lead to the faster decay curves, consistent with the simple calculations using Equation (9) and shown in Figure 5. If we solve Equation (9) and fit the result numerically to all three curves shown, we obtain the parameters $k_{\text{ext}} = (4.78 \pm 0.43) \times 10^{-11} \text{cm}^3 \text{s}^{-1}$, $C = (8.83 \pm 1.57) \times 10^{-29} \text{cm}^6 \text{s}^{-1}$, $\tau_n = 511 \pm 80$ ns, and $\tau_p = 871 \pm 251$ ns. Note that the values for $k_{\text{rad}}(1 - p_r) = k_{\text{ext}}$ directly result from a fit of the data. If we want to determine k_{rad} separately, we need to obtain an estimate of the reabsorption probability first, which can be done analytically for a film on glass. Under the reasonable assumption that in this case there is no parasitic absorption, the term $1 - p_r$ is equal to the emission probability p_e , which can be calculated from the equation.^[82]

$$p_e = \frac{2 \int_0^\infty a(E) \phi_{\text{BB}}(E) dE}{d \int_0^\infty 4 n_r^2(E) \alpha(E) \phi_{\text{BB}}(E) dE} \quad (17)$$

The idea of this equation is that the denominator contains the terms that lead to photon generation inside the volume of the perovskite film, that is, Equation (10) multiplied with film thickness. Hence, the denominator depends on the absorption coefficient α . Here photons are generated and emitted into the 4π solid angle inside the perovskite film. The numerator provides the flux that is emitted into air ($n_r = 1$) from a planar surface (Equation (15)) which lacks the $4n_r^2$ term of the denominator and it depends on the absorptance a instead of the absorption coefficient α . In case of a film on glass, there are two surfaces at which light can outcouple, so there is a factor of 2 in the numerator accounting for the two emitting surfaces. In total, we can estimate the emission probability to be about 5% for a flat film on glass, which then leads to the values of $k_{\text{rad}} = (8.77 \pm 0.79) \times 10^{-10} \text{cm}^3 \text{s}^{-1}$. We note that smaller k_{rad}

values are obtained if a second order non-radiative recombination is considered, as discussed in Section 3.3 (Table 4). Using such analysis we obtain values for $k_{\text{rad}} = 6 \times 10^{-11} \text{cm}^3 \text{s}^{-1}$, which also will be shown in Section 6 to be in much better agreement with experimental Q_e^{lum} versus lifetime values from literature. Therefore, for consistency, we will use a $k_{\text{rad}} = 6 \times 10^{-11} \text{cm}^3 \text{s}^{-1}$ for all calculated radiative recombination data in this manuscript. We also note that the effect of surface roughness is included in Equation (17) in the absorptance a in the numerator of the equation. If the surface becomes rougher, the absorptance increases and thereby p_e increases.^[93,94]

Therefore in order to obtain recombination parameters relevant for solar cell operation, excitation densities close to AM1.5G conditions should be used for the TRPL measurement. However, before measuring and analyzing the data, the photoexcited (steady-state) carrier density corresponding to solar cell operation is not known, since it requires knowledge of the minority carrier lifetime. This means that in transient PL measurements always a series of different excitation conditions should be used, spanning a wide range. Considering typical lifetimes obtained for halide perovskite samples of 100 ns–1 μs , a typical injected carrier density required in the TRPL experiment can be estimated at $\Delta n = \phi \times \tau/d \approx 4 \times 10^{14} - 4 \times 10^{15} \text{cm}^{-3}$ assuming a thickness $d = 400$ nm.

To summarize, we notice that the general trend of the fluence-dependent behavior follows from the combination of different recombination mechanisms and does not require adjusting any parameter between the three decay curves. The result also highlights the necessity to measure at different laser fluences if all recombination parameters should be extracted from the transient data. We also note that the extracted value for k_{rad} is consistent with the range of values given in Section 4.1 and is compatible with an effective DOS $N_c \times N_v = 4.9 \times 10^{36} \text{cm}^{-6}$ and an effective mass of $m^* = 0.2$.

The monomolecular lifetime of ≈ 500 ns can be interpreted in two different ways. One option is that bulk recombination dominates the terms of the recombination rate that scale linearly with the minority carrier concentration. In this case, the decay seen for longer times in all three decays in Figure 8 would be identical to the average of the lifetimes $(\tau_p + \tau_n)/2$ introduced in Section 3.2.2. However, there is also an alternative interpretation possible. The surface of the film might dominate monomolecular recombination, then the lifetime is obtained as discussed in the following section.

4.3. Surface Recombination

In most inorganic semiconductors, surfaces or interfaces are among the most critical areas accelerating recombination in a device.^[95,96] The reason for this is that the crystal structure of one material ends at its surface or at the interface to another layer. In many cases, the surface forms dangling bonds that create electronic states in the band gap. The normal strategy to circumvent this problem is to apply passivation layers that move the electronic states in the band gap out of the band gap by forming new molecular orbitals at the interface. A classic example is the surface of a silicon wafer that contains Si atoms where at least one of the four valence electrons does not form

a bond with a valence electron from another Si atom. In this case, passivation layers from, for example, amorphous Si could provide either additional bonds to valence electrons in amorphous Si or they provide hydrogen atoms that attach to dangling bonds and thereby also make sure that there are no unsaturated bonds.^[96] In the case of perovskites, the same problem exists, however to a slightly lesser degree of severity as in most inorganic materials. In the same way as the bulk material forms mostly shallow defects, theoretical calculations by Uratani et al.^[97] show that this is also true for the surfaces of MAPi. Hence, the defects formed at surfaces are likely much less detrimental than in most covalent semiconductors where dangling bonds form deep defects. In addition, the surfaces of lead-halide perovskites can quite easily be passivated by, for example, exposure to oxygen,^[86] by covering them with various organic layers^[65,84,85,98] or by using 2D perovskites or wide band gap perovskites as surface passivation layers.^[99–101]

Nevertheless, we have to include the possibility of recombination at the surface or interface of any of our perovskite films or layer stacks used in photoluminescence experiments. Surface recombination is typically treated as a boundary condition to the electron and hole concentrations in the continuity equations (Equations (1) and (2)) introduced earlier. The boundary condition for electrons can be expressed as

$$\pm D_n \left. \frac{dn}{dx} \right|_{x=0,d} = \frac{np - n_i^2}{n/S_p + p/S_n} \Big|_{x=0,d} \quad (18)$$

where the positive sign is for $x = 0$ and the negative sign for $x = d$. Thus, if the concentration of electrons decreases toward the back contact at $x = d$ ($dn/dx < 0$), this has to correspond to a positive rate of recombination at that contact. Here, S_n and S_p are the surface recombination velocities for electrons and holes and thereby fulfill a similar role as the (inverse) electron and hole lifetimes in bulk SRH recombination (see Table 3).

In order to fully simulate the effect of surface recombination on a photoluminescence transient, it is necessary to know the carrier concentrations at the interfaces or surfaces (i.e., at $x = 0$ and $x = d$) as a function of time. Hence one has to solve the full system of differential equations (continuity equation for electrons and holes and the Poisson equation) as a function of position and time, which is however not possible analytically. In case of many traditional doped semiconductors, there is a relatively simple solution for the problem. As long as one restricts the problem to low-level injection, the mathematical problem reduces to solving only the continuity equation for minority carriers as a function of position and time with the boundary condition (assuming a p-type layer).

$$\pm D_n \left. \frac{dn}{dx} \right|_{x=0,d} = S_n n \Big|_{x=0,d} \quad (19)$$

The solution of the differential equation in position and time then becomes a Fourier series. At long times, the decay will follow the first term of the Fourier series^[102,103] with the characteristic decay time.

$$\tau_s = \frac{d}{2S_n} + \frac{d^2}{D_n \pi^2} \quad (20)$$

Here, we assume that the surface recombination velocities are the same for both interfaces. The two terms on the right-hand side of Equation (20) are related to i) the actual recombination process at the interface limited by the magnitude of the surface recombination velocity S_n and ii) the transport to the surface which scales quadratically with thickness and inversely with the diffusion constant D_n . Thus, for higher mobilities and smaller distances the second term would vanish and the first one would dominate. However, for large thicknesses and high values of the surface recombination velocity, also the first term may vanish and the second one may dominate the result. A typical example for the latter scenario would be an unpassivated bare Si wafer, whose effective lifetime would not fall below about 1 μ s (if the surface limits the lifetime), because of the second term in Equation (20).^[104]

In the case of perovskites, photoluminescence experiments are likely done mostly in high-level injection and the analytical treatment of the problem is rather difficult. However, we may numerically calculate which monomolecular lifetime is expected for a layer with infinitely long bulk lifetime as a function of surface recombination velocity and thickness. Figure 9 shows the result of this calculation. On the bottom right, we note the diffusion limited regime, that is, the lifetimes that are so short that they are physically impossible, because transport to the surface would not be fast enough. These lifetimes are however much smaller than what we measure experimentally which suggests that it is essentially the $d/2S$ term that is relevant for perovskites.

If we use the $\tau \approx 500$ ns obtained experimentally from the data shown in Figure 8, we arrive at the conclusion that the two remaining surfaces (glass/perovskite and perovskite/ N_2 (g)) must have surface recombination velocities of 10 cm s^{-1} or lower (note the sample is in a nitrogen filled sample holder). Any higher surface recombination velocities would be inconsistent with the observed long lifetimes.

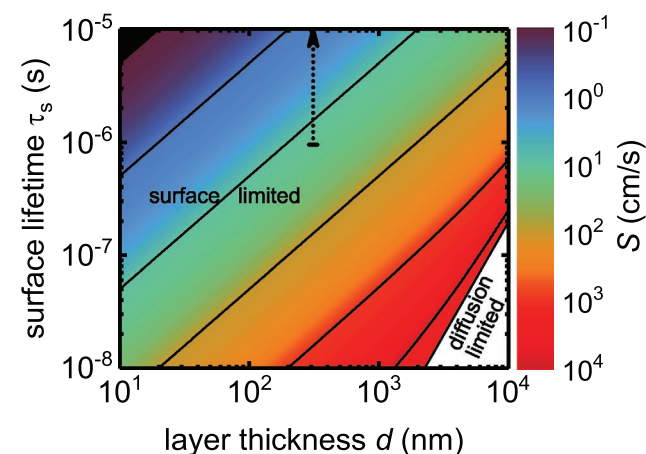


Figure 9. Surface recombination velocity as a function of the surface lifetime τ_s and the layer thickness d of a MAPi sample on glass. The calculation assumes a mobility of $20 \text{ cm}^2 \text{ V}^{-1} \text{ s}^{-1}$ for electrons and holes and equal surface recombination velocities S at the two surfaces of the sample. The blank area in the lower right corner marks the mathematically impossible region where the lifetime is increased by the finite speed of charge-carrier diffusion toward the surfaces. The dotted black line indicates the possible surface lifetimes for the observed layer thickness of $d = 311$ nm in the sample shown in Figure 8. Reproduced with permission.^[94] Copyright 2016, The American Physical Society.

4.4. Parasitic Absorption

In Section 4.2, we observed that the radiative recombination coefficient k_{rad} can only be determined from the data if we account for the probabilities of reabsorption and emission of light. In reality, k_{rad} is fixed by the properties of the material such as the absorption coefficient and the density of states. What changes with the amount of light being reabsorbed is the observed bimolecular rate constant $k_{\text{rad}}(1 - p_r)$. Hence, by modulating the amount of light that is parasitically absorbed it is possible to change the observed bimolecular rate constant. **Figure 10** shows an example of data that was obtained using layers grown on a Si wafer using either a thick or a thin SiO_x layer in between the Si wafer and the perovskite layer.^[53] In case of the thin SiO_x layer, light impinging on the back contact can easily couple into the Si wafer where it is then absorbed and cannot contribute to reabsorption in the perovskite (quantified by the probability p_r) anymore. In case of a thick SiO_x layer, more light is reflected back into the perovskite and is reabsorbed. Consequently, we observe different values for $k_{\text{rad}}(1 - p_r)$ despite the fact that the films are prepared in the exact same way, assuming that there is no change in k_{rad} between the two samples.

5. Layer Stacks and Devices

5.1. Steady-State PL

One of the key challenges in optimizing perovskite solar cells is to choose the best transport layers for a given perovskite composition. Transport layers essentially have to fulfill two criteria,

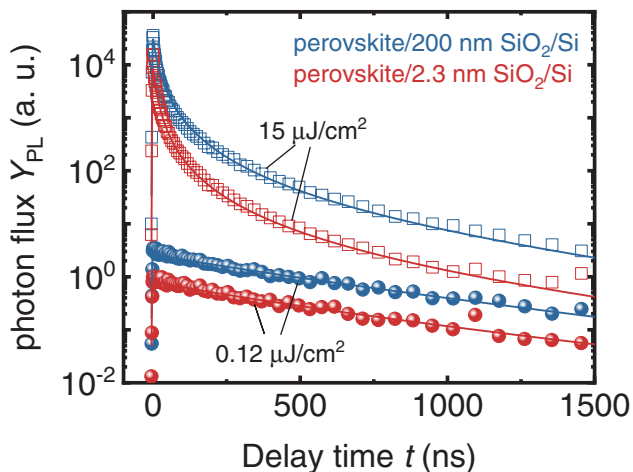


Figure 10. PL decays for different excitation conditions and for two different sample geometries namely a MAPI film on a thick, reflecting SiO_2 layer (blue) and a MAPI film on a very thin SiO_2 layer (red) that allows light incoupling into the underlying Si wafer. The decay at higher fluences and short times, where radiative recombination becomes important, is faster for the thin SiO_2 . This is consistent with the expectation that the additional parasitic absorption leads to less photon recycling and therefore a faster effective radiative recombination coefficient $k_{\text{ext}} = k_{\text{rad}}(1 - p_r)$. See Table 4 and ref. [53] for the values that were used to fit the curves. Adapted with permission.^[53] Copyright 2017, American Chemical Society.

namely they have to ideally do the job of a passivation layer (i.e., reduce non-radiative recombination at the perovskite surface) while at the same time allow efficient charge extraction. Steady-state photoluminescence can be used to screen transport layers for their ability to maintain a high photoluminescence.^[19] Any reduction in photoluminescence intensity when adding charge extraction layers to a perovskite absorber layer is detrimental for the V_{oc} and therefore it is not possible to use steady-state photoluminescence quenching at open circuit as a good indicator of efficient charge transfer to the electron or hole transport layer. It is also interesting to note, while the PL of a solar cell or a solar cell stack has to be maximized under open-circuit conditions; at applied voltages substantially below open-circuit, the PL should be rapidly quenched with respect to the PL at V_{oc} , as charges need to be efficiently extracted prior to recombination.^[14]

Much of the usefulness of photoluminescence characterization in solar cell development comes from the possibility to predict or compare the open-circuit voltage measured on a device with the quasi-Fermi level splitting derived from the photoluminescence measurements. In addition to the possibilities to estimate ΔE_F as given above (Equation (15)), there is also a direct relationship between the external quantum efficiency Q_e^{lum} of photoluminescence emission and the quasi-Fermi level splitting in a device.^[68,70]

$$\Delta E_F = \Delta E_f^{\text{rad}} + kT \ln \{ Q_e^{\text{lum}} \} \quad (21)$$

Here, the radiatively limited ΔE_f^{rad} refers to the maximally achievable V_{oc} in the absence of non-radiative (defect) recombination.

The steady-state photoluminescence can be used to quantify the internal voltage or quasi Fermi level splitting ΔE_f in perovskite layers with or without attached transport layers as well as in complete cells allowing a direct comparison with the device V_{oc} . An example of this is shown in **Figure 11** where the Q_e^{lum} is shown for a neat triple cation perovskite layer on glass and in contact with the electron and hole transport layers (ETL and HTL) and in the full device stack. The analysis reveals a drop of the ΔE_f and Q_e^{lum} values when the perovskite is in contact with either of the transport layers revealing losses due to interface recombination in both sides. This analysis allowed us to optimize the device architecture with the use of interlayers where both, the measured quasi-Fermi level splitting and the V_{oc} of the devices were increased with the passivation. This has been shown to provide very consistent results in several recent studies being of great help for the understanding of the limiting device components and the development of more efficient devices.^[8,19,33] However, it has also been found that in some cells with poor-performing transport layers (such as PEDOT:PSS and P3HT) the internal ΔE_f in the cell or the optical pin-stack on glass can be higher than the external qV_{oc} . This implied that the hole (or electron) quasi-Fermi level bends in a specific region in the device, which we attributed to a misalignment of the energy levels of the transport layer and the perovskite.^[13,19] Note that open-circuit voltage losses due to non-ideal band alignment between absorber and contact layers are expected to vary substantially if absorber layers with other stoichiometries and in particular

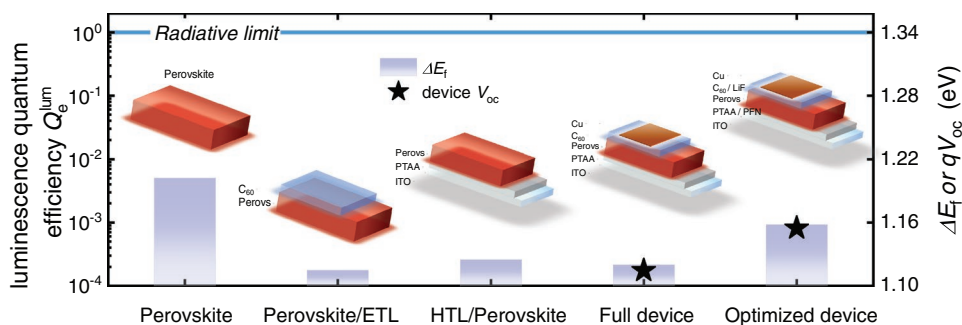


Figure 11. External photoluminescence quantum yield Q_e^{lum} for different layer stacks covering a pristine perovskite layer on glass, a perovskite in contact with the ETL (C_{60}), a perovskite in contact with the HTL (PTAA), a full non-passivated device stack, and an optimized device stack with interlayers (LiF and PFN). The calculated quasi-Fermi level splitting and the open circuit voltage measured on the devices (star symbols) are shown in the right axis. Data from ref. [8].

band gaps are used. Lower band gap perovskites for instance function well with PEDOT:PSS and C_{60} ,^[105] while the typical ~ 1.6 eV band gap compositions usually show severe losses in combination with PEDOT:PSS and still some losses with C_{60} .^[19]

5.2. Transient PL

Further quantitative information on the recombination processes in layer stacks can be obtained from transient photoluminescence measurements. In these measurements charge transfer can play a significant role in addition to interface and bulk recombination since during transient measurements, substantial currents can flow to equilibrate the quasi-Fermi levels. In order to understand the mechanisms taking place during such a transient, let us study **Figure 12**,^[30] where TRPL transients where numerically simulated. The upper row of figures (panel a) and b)) show the PL transients and the differential lifetime $\tau_{\text{diff}}(t) = -(\text{dln}(Y_{\text{pl}}(t))/\text{d}t)^{-1}$, respectively, for a situation with a comparatively low laser fluence (1 nJ cm^{-2}) corresponding to an injected carrier density of $1.3 \times 10^{14} \text{ cm}^{-3}$ (excitation wavelength $\lambda = 496 \text{ nm}$). Photons of the laser pulse are absorbed mainly in the perovskite absorber layer that we assume to be interfaced with a PCBM electron transport layer. Within a relatively short period of $< 1 \text{ ns}$, the electrons and holes will have been able to diffuse through a 300 nm thick perovskite film. Hence equilibration within the absorber layer will happen on timescales that are not resolved by the transient shown. Subsequently, electrons transfer from the perovskite to the PCBM. Because this reduces the product np of electron and hole concentrations in the absorber, the photoluminescence drops quickly (see initial decay in panel a)) on a timescale of $10\text{--}50 \text{ ns}$. Once electrons are transferred to the PCBM, they cannot be extracted (the sample is not contacted) but may recombine with holes in the perovskite. The speed of this recombination can be expressed by an interfacial recombination velocity S_R that is varied in Figure 12a) to show how it affects the transients at longer times. At low fluences, the two decays caused by electron transfer to the PCBM and interfacial recombination are neatly separated and the limiting non-radiative recombination lifetime (either bulk or interface) can be extracted from the slower decay (τ_2).

This situation changes, when we assume higher fluences in the simulation ($1 \mu\text{J cm}^{-2}$ corresponding to an injected carrier density of $1.3 \times 10^{17} \text{ cm}^{-3}$). The results are shown in the second row of Figure 12 (panels c) and d)). Initially, the electrons will still transfer quickly to the PCBM. However, soon the electron transfer slows down because electrons accumulate in the PCBM and thus reduce the efficiency of further electron transfer. Due to the higher fluence, the amount of charge that can be stored in the PCBM will become relevant for the shape of the decay. This density of electrons stored in the PCBM depends on the rate of electron transfer to the PCBM, the rate of recombination and at the perovskite-PCBM interface and also on the conduction band offset between the two materials. The latter governs the rate of back transfer of electrons from the PCBM to the perovskite. Hence, since for high fluences a combination of different parameters affects the transient, the extraction of those parameters from the transient becomes challenging. Especially at high fluences that are often necessary for a good signal to noise ratio, analytical equations will not be able to describe the decay and numerical simulations have to be used to analyze experimental data. Examples for such an analysis are published in ref. [30].

Fluence-dependent TRPL transients corresponding to the photoluminescence quantum efficiency measurements shown in Figure 11 are presented in **Figure 13** for a perovskite film with a C_{60} electron transport layer (symbols in different shades of blue). For comparison, the PL transient of the pristine perovskite film measured with a fluence of 30 nJ cm^{-2} ($1.8 \times 10^{15} \text{ cm}^{-3}$) is shown (green symbols). It can be seen that after an initial faster decay at times $> 10 \text{ ns}$, the photoluminescence of the stack decays exponentially with a decay time of $\approx 20 \text{ ns}$, while the pristine perovskite film on glass shows a decay time of 330 ns . Applying Equation (20), an upper bound of the surface recombination velocity of $S_R = 40 \text{ cm s}^{-1}$ and $S_R = 1000 \text{ cm s}^{-1}$ can be given for the pristine layer and stack, respectively. The corresponding quasi-Fermi level splitting can be estimated from the measured lifetime (two times the decay time in high injection) using Equation (5), with $n_i^2 = 8.3 \times 10^{10} \text{ cm}^{-6}$ which gives values of $\Delta E_f = 1.06 \text{ eV}$ and $\Delta E_f = 1.21 \text{ eV}$, respectively. Comparison with the results from the steady-state analysis in Figure 11 indicates a relatively good agreement with the quasi-Fermi level splitting values obtained in those measurements.

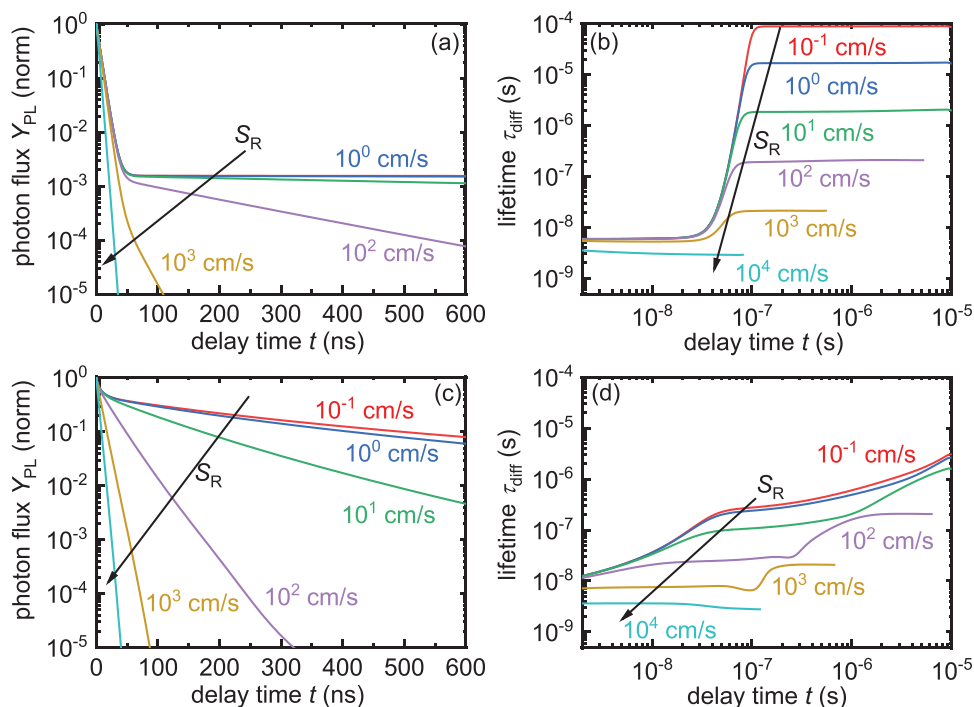


Figure 12. a) Photoluminescence decay of a MAPI film interfaced with a PCBM electron transport layer simulated for different values of the surface recombination velocity S_R ranging from $S_R = 1 \text{ cm s}^{-1}$ to $S_R = 10^4 \text{ cm s}^{-1}$ and assuming extremely low excitation conditions of 1 nJ cm^{-2} . b) Differential lifetime determined from the data in (a) but for high excitation of 1000 nJ cm^{-2} . Now, charge accumulation in the PCBM slows down charge transfer to the PCBM. Instead of the distinct two phasic decay seen in (a) that was determined by fast charge extraction and slow or fast recombination (depending on the value of S_R), the situation at high fluences shows a more smeared out decay where also the charge extraction depends on the value of the surface recombination velocity. d) Differential lifetime determined from the data in (c). The parameters used for the simulation are found in the Supporting Information of ref. [30]. Adapted with permission.^[30] Copyright 2018, The Royal Society of Chemistry.

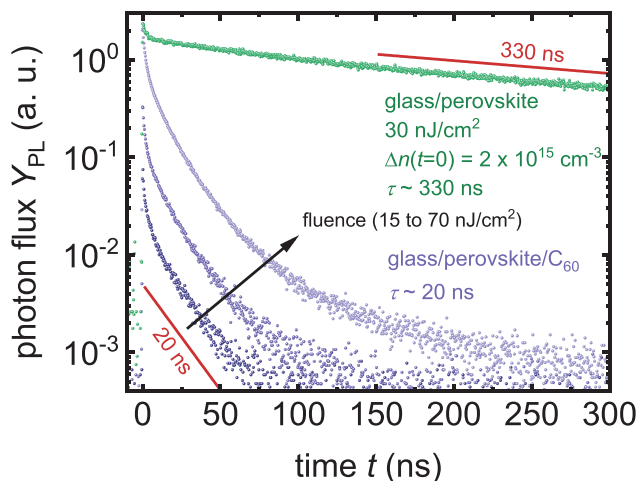


Figure 13. Fluence-dependent TRPL measurements of a perovskite/ C_{60} stack. The curves qualitatively agree with each other, indicating that neither radiative recombination nor fluence-dependent charge extraction limits the carrier decay. A decay time of 20 ns can be extracted from the exponential regime for time delays $> 10 \text{ ns}$. This corresponds to an effective SRH-lifetime of 40 ns, since the excitation density of 10^{15} cm^{-3} corresponds to high level injection for these samples. Also shown is the TRPL decay for the perovskite film on glass measured at an excitation intensity of $2 \times 10^{15} \text{ cm}^{-3}$, yielding a decay time of $\approx 330 \text{ ns}$, corresponding to a SRH-lifetime of 660 ns. Data from ref. [8].

6. The Relation between Lifetime, Luminescence Quantum Efficiency, and Quasi-Fermi Level Splitting

In Section 3.5, we have introduced the concept of the external luminescence quantum efficiency which depends on the rates of radiative and non-radiative recombination and on the optical properties of the sample (defined by p_e , p_v and p_a). Equation (14) explicitly presents the relation between the lifetime τ and the external PL quantum yield Q_e^{lum} in the quite relevant limit that SRH recombination is the dominant non-radiative recombination term. Given that every change in $kT \ln(Q_e^{\text{lum}})$ results in a corresponding change in qV_{oc} through Equation (21), we can find relations between both the lifetime and Q_e^{lum} and the lifetime and qV_{oc} . Several parameters discussed throughout this tutorial affect this relation including the internal radiative recombination coefficient k_{rad} , the equilibrium charge-carrier concentration p_0 (for the arbitrary example of a p-type semiconductor) and the probabilities p_e and p_a of emission and parasitic absorption of internally generated photons. From Table 4 we have observed that the reported values for k_{rad} in literature vary by more than one order of magnitude, even though k_{rad} is an intrinsic material property and should be therefore a constant. This can present challenges to estimate the relation between lifetimes and PL quantum efficiencies with accuracy. We additionally note that halide perovskites are considered to be

relatively intrinsic semiconductors generally exhibiting doping concentrations (and hence values for p_0) lower than 10^{15} cm^{-3} .

If the relations of the previously mentioned parameters are understood and with a relatively good knowledge of their values, a consistent picture of ΔE_f , Q_e^{lum} , V_{oc} and lifetimes τ measured for film stacks and devices with consistent measurement conditions and correct analytical or numerical analysis should be achieved. As mentioned earlier, lifetime measurements on stacks and devices can be challenging, thus a direct comparison of steady-state and transient luminescence measurements works best for pristine perovskite layers deposited without charge transport layers or contacts. However, we note that although the quasi-Fermi level splitting can be estimated from these measurements, it cannot be directly verified with open-circuit measurements.

In Figure 14a we show various experimental values from literature for the device V_{oc} versus the reported photoluminescence lifetime τ , which would, in high-level injection, correspond to $(\tau_p + \tau_n)/2$. Also shown are curves calculated using Equations (S1) and (S2), Supporting Information, for $V_{\text{oc}}^{\text{Rad}} = 1.324 \text{ V}$, $k_{\text{rad}} = 6 \times 10^{-11} \text{ cm}^3 \text{ s}^{-1}$ and different doping densities p_0 . It can be seen that the reported V_{oc} values often yield significantly lower values than expected from the lifetime as compared with the theoretical curves. This may be due to the fact that for some of the data from literature, the measurement conditions were not matched for the lifetime and ΔE_f and V_{oc} measurements, and/or that the extracted lifetime values were not representative due to inadequate analysis or measurement conditions as discussed earlier. For example, if lifetimes are measured on perovskite films on glass but the V_{oc} is measured on a device, additional interface recombination in the device would not have been accounted for in the PL transient. Therefore, we would expect the data points to lie generally below or on the black line for the case of intrinsic absorber layers (blue shaded region). This is the case for the majority of data points with a minority of outliers being slightly above the black and blue solid lines. Another reason for V_{oc} values falling below

the expected theoretical curves can be a mismatch between the internal and external voltage of the device. Although in general it is assumed that the internal quasi-Fermi level splitting determined by the level of non-radiative recombination equals the externally observed open-circuit voltage, this is not necessarily true for all device configurations as reported in several recent studies.^[13,19] In particular, a large band offset for holes at the p-interface has been found to lead to voltage reductions of up to 150 mV compared to the quasi-Fermi level splitting obtained from luminescence.

Figure 14b shows the experimental PL quantum yield values Q_e^{lum} versus SRH lifetimes τ for halide-perovskite layers, stacks or devices together with theoretical curves obtained with Equation (S1), Supporting Information. The dependence of the experimentally observed PL quantum yield on carrier lifetime agrees reasonably well with the theoretically expected curves (calculated with the same values as in Figure 14b), with some outliers for which the Q_e^{lum} is substantially higher than what is expected from the reported carrier lifetime. Also, a reduction of Q_e^{lum} at long lifetimes τ is expected when the parasitic absorption probability p_a is not equal to zero. This limits the maximum achievable Q_e^{lum} that can be achieved for a given lifetime. For carrier lifetimes $< 1 \mu\text{s}$, an increased doping density can explain larger values of Q_e^{lum} , as observed for example for GaAs,^[118] and similar effects of doping have recently been shown in halide perovskites.^[119] However, the figure also shows that even if high doping is assumed, for external PL quantum yield values exceeding 1%, lifetimes above $1 \mu\text{s}$ should be observed, which is contrast with at least some of the data points in Figure 14. This could be due to problems with either the quantum efficiencies or the lifetime analysis, potentially because non-identical samples were investigated for both measurements, or because samples degraded during or before the lifetime measurement. Since large external quantum efficiencies are an indication of superior material quality and naturally draw significant interest in the community, we therefore suggest that if large $Q_e^{\text{lum}} > 1\%$ are reported for perovskite thin films, efforts should be

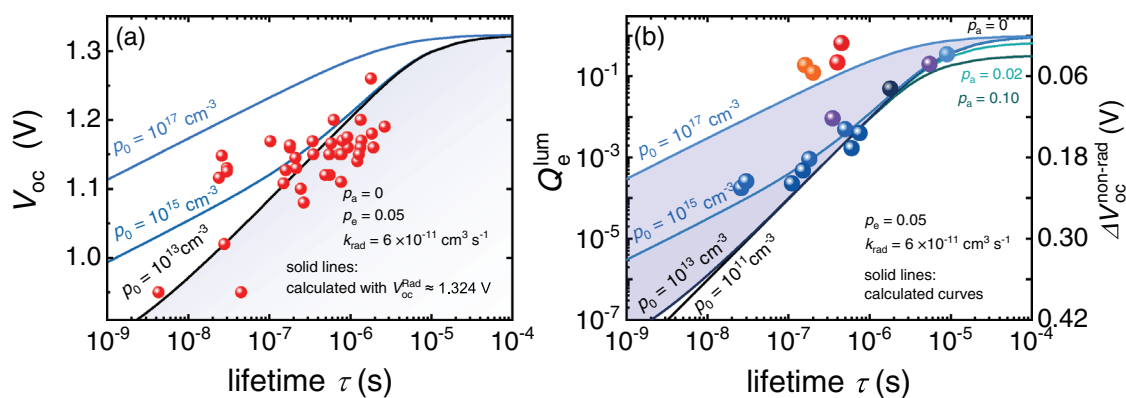


Figure 14. a) Experimental values of device V_{oc} and corresponding reported lifetimes τ (see Table S1, Supporting Information) that were derived from PL transients measured on films with or without contacts.^[8,33,106–113] In high level injection these lifetimes correspond to $(\tau_p + \tau_n)/2$ (see Section 4.2). Calculated curves for a planar 500 nm thick film with the parameters stated in the figure for equivalent 1 sun conditions of perovskites absorbers with $p_0 = 10^{15} \text{ cm}^{-3}$ and 10^{17} cm^{-3} (blue lines) are also shown. We note that the theoretical curves are calculated for a $V_{\text{oc}}^{\text{Rad}}$ of 1.324V, which corresponds to perovskite films with a bandgap energy of $\approx 1.60 \text{ eV}$. This is in accordance with the experimental data shown in the figure (see Table S1, Supporting Information). b) Experimental values of the external photoluminescence quantum efficiency Q_e^{lum} measured at 1 sun equivalent conditions reported in literature with the corresponding PL lifetime τ (see Table S2, Supporting Information).^[8,33,65,84,114–117] The black line is the calculated curve using Equation (14) for various values of p_0 and for different values of the parasitic absorption probability p_a . The right axis shows the voltage loss due to non-radiative recombination $\Delta V_{\text{oc}}^{\text{nonRad}}$ for a given value of Q_e^{lum} as calculated from the second term of Equation (21).

undertaken to back these values up with lifetime values measured under equivalent conditions.

The given calculated curves assume an absorber thickness of 500 nm, escape probability of 5%, and radiative constant $k_{\text{rad}} = 6 \times 10^{-11} \text{ cm}^3 \text{ s}^{-1}$, consistent with previous figures shown in this manuscript. However, as also discussed in previous sections the exact value of the radiative constant is still debated, and device thickness as well as escape probability of photons may vary for different samples. To illustrate the effect of these parameters on the expected quantum efficiency versus lifetime curves, several plots are shown in the Supporting Information.

7. Conclusions

While PL characterization is routinely used in the perovskite solar cell community, the results are often challenging to interpret and much more has to be learned, for example with respect to the interplay between charge extraction and recombination. Moreover, standards in measuring and reporting results from photoluminescence-based measurements are missing which often complicates a direct comparison between PL results obtained from different groups or different compositions. This obscures how certain kinetic properties in the bulk or the interfaces correlate to the open-circuit voltage or other performance parameters in steady-state.

In this tutorial, we have discussed the application of transient and steady-state PL measurements to neat perovskite films and solar cell stacks in the presence of transport layers and metal electrodes (complete cells). To this end, we provided details on PL measurement setups along with an introduction into the basic principles to determine the charge-carrier lifetime and recombination rate constants under different conditions, ranging from low to high level injection, the presence of background doping, and charge extracting layers relevant to real devices. We then discussed the impact of photon recycling and parasitic absorption on the obtained bimolecular recombination coefficient and its impact on the device performance. Importantly, a direct comparison of transient and steady-state PL results as obtained on different perovskite layer stacks demonstrates that kinetic parameters can well describe the operation of perovskite solar cells in steady-state (analytically as well as numerically); given that they are measured under relevant conditions. However, a survey of literature in some cases shows significant inconsistencies between the kinetic parameters, such as the carrier lifetime and the obtained radiative efficiencies or open-circuit voltage in steady-state that have to be further explored. In the future, we anticipate that a more accurate determination of bulk and interfacial charge transfer and recombination rate constants will improve our understanding of perovskite solar cell operation even further, which will be an important contribution to approach the thermodynamic efficiency limit in perovskite solar cells.

Supporting Information

Supporting Information is available from the Wiley Online Library or from the author.

Acknowledgements

T.K. acknowledges the Helmholtz Association for funding via the PEROSEED project. This work was in part funded by HyPerCells (a joint graduate school of the Potsdam University and the HZB) and M.S. also acknowledges the Deutsche Forschungsgemeinschaft (DFG, German Research Foundation)—project number 423749265 – SPP 2196 (SURPRISE) for funding.

Conflict of Interest

The authors declare no conflict of interest.

Keywords

metal halide perovskites, numerical simulations, photoluminescence, photon recycling

Received: December 16, 2019

Revised: February 22, 2020

Published online: May 6, 2020

- [1] B. R. C. Efficiencies, <https://www.nrel.gov/pv/cell-efficiency.html>, (accessed: April 2020).
- [2] Y. Rong, Y. Hu, A. Mei, H. Tan, M. I. Saidaminov, S. I. Seok, M. D. McGehee, E. H. Sargent, H. Han, *Science* **2018**, *361*, eaat8235.
- [3] N.-G. Park, *Adv. Energy Mater.* **2019**, *10*, 1903106.
- [4] J. P. Correa-Baena, M. Saliba, T. Buonassisi, M. Grätzel, A. Abate, W. Tress, A. Hagfeldt, *Science* **2017**, *358*, 739.
- [5] L. Krückemeier, U. Rau, M. Stolterfoht, T. Kirchartz, *Adv. Energy Mater.* **2020**, *10*, 1902573.
- [6] A. K. Jena, A. Kulkarni, T. Miyasaka, *Chem. Rev.* **2019**, *119*, 3036.
- [7] S. Akin, N. Arora, S. M. Zakeeruddin, M. Grätzel, R. H. Friend, M. I. Dar, *Adv. Energy Mater.* **2019**, *9*, 1903090.
- [8] M. Stolterfoht, C. M. Wolff, J. A. Marquez, S. Zhang, C. J. Hages, D. Rothhardt, S. Albrecht, P. L. Burn, P. Meredith, T. Unold, D. Neher, *Nat. Energy* **2018**, *3*, 847.
- [9] V. Sarritzu, N. Sestu, D. Marongiu, X. Chang, S. Masi, A. Rizzo, S. Colella, F. Quochi, M. Saba, A. Mura, G. Bongiovanni, *Sci. Rep.* **2017**, *7*, 44629.
- [10] A. D. Wright, C. Verdi, R. L. Milot, G. E. Eperon, M. A. Perez-Osorio, H. J. Snaith, F. Giustino, M. B. Johnston, L. M. Herz, *Nat. Commun.* **2016**, *7*, 11755.
- [11] J. A. Steele, P. Puech, B. Monserrat, B. Wu, R. X. Yang, T. Kirchartz, H. Yuan, G. Fleury, D. Giovanni, E. Fron, M. Keshavarz, E. Debroye, G. Zhou, T. C. Sum, A. Walsh, J. Hofkens, M. B. J. Roelofs, *ACS Energy Lett.* **2019**, *4*, 2205.
- [12] Y. Guo, O. Yaffe, T. D. Hull, J. S. Owen, D. R. Reichman, L. E. Brus, *Nat. Commun.* **2019**, *10*, 1175.
- [13] P. Caprioglio, M. Stolterfoht, C. M. Wolff, T. Unold, B. Rech, S. Albrecht, D. Neher, *Adv. Energy Mater.* **2019**, *9*, 1901631.
- [14] M. Stolterfoht, V. M. Le Corre, M. Feuerstein, P. Caprioglio, L. J. A. Koster, D. Neher, *ACS Energy Lett.* **2019**, *4*, 2887.
- [15] N. Wu, Y. Wu, D. Walter, H. Shen, T. Duong, D. Grant, C. Barugkin, X. Fu, J. Peng, T. White, K. Catchpole, K. Weber, *Energy Technol.* **2017**, *5*, 1827.
- [16] G. El-Hajje, C. Momblona, L. Gil-Escrig, J. Ávila, T. Guillemot, J.-F. Guillemoles, M. Sessolo, H. J. Bolink, L. Lombez, *Energy Environ. Sci.* **2016**, *9*, 2286.

- [17] S. D. Stranks, V. M. Burlakov, T. Leijtens, J. M. Ball, A. Goriely, H. J. Snaith, *Phys. Rev. Appl.* **2014**, 2, 034007.
- [18] S. D. Stranks, G. E. Eperon, G. Grancini, C. Menelaou, M. J. P. Alcocer, T. Leijtens, L. M. Herz, A. Petrozza, H. J. Snaith, *Science* **2013**, 342, 341.
- [19] M. Stollerfoht, P. Caprioglio, C. M. Wolff, J. A. Marquez, J. Nordmann, S. Zhang, D. Rothhardt, U. Hörmann, Y. Amir, A. Redinger, L. Kegelman, F. Zu, S. Albrecht, N. Koch, T. Kirchartz, M. Saliba, T. Unold, D. Neher, *Energy Environ. Sci.* **2019**, 12, 2778.
- [20] X. Wu, M. T. Trinh, D. Niesner, H. Zhu, Z. Norman, J. S. Owen, O. Yaffe, B. J. Kudisch, X. Y. Zhu, *J. Am. Chem. Soc.* **2015**, 137, 2089.
- [21] S. Singh, C. Li, F. Panzer, K. L. Narasimhan, A. Graeser, T. P. Gujar, A. Köhler, M. Thelakkat, S. Huettner, D. Kabra, *J. Phys. Chem. Lett.* **2016**, 7, 3014.
- [22] C. Li, A. Guerrero, S. Huettner, J. Bisquert, *Nat. Commun.* **2018**, 9, 5113.
- [23] S. Bai, P. Da, C. Li, Z. Wang, Z. Yuan, F. Fu, M. Kawecki, X. Liu, N. Sakai, J. T.-W. Wang, S. Huettner, S. Buecheler, M. Fahlman, F. Gao, H. J. Snaith, *Nature* **2019**, 571, 245.
- [24] F. Staub, H. Hempel, J. C. Hebig, J. Mock, U. W. Paetzold, U. Rau, T. Unold, T. Kirchartz, *Phys. Rev. Appl.* **2016**, 6, 044017.
- [25] C. M. Wolff, F. Zu, A. Paulke, L. P. Toro, N. Koch, D. Neher, *Adv. Mater.* **2017**, 29, 1700159.
- [26] T. S. Sherkar, C. Momblona, L. Gil-Escrig, H. J. Bolink, L. J. A. Koster, *Adv. Energy Mater.* **2017**, 7, 1602432.
- [27] T. S. Sherkar, C. Momblona, L. Gil-Escrig, J. Ávila, M. Sessolo, H. J. Bolink, L. J. A. Koster, *ACS Energy Lett.* **2017**, 2, 1214.
- [28] R. K. Ahrenkiel, in *Minority Carriers in III-V Semiconductors: Physics and Applications* (Eds: R. K. Ahrenkiel, M. S. Lundstrom), Academic Press Inc., San Diego **1993**, p. 39.
- [29] M. Maiberg, R. Scheer, *J. Appl. Phys.* **2014**, 116, 123711.
- [30] B. Krogmeier, F. Staub, D. Grabowski, U. Rau, T. Kirchartz, *Sustainable Energy Fuels* **2018**, 2, 1027.
- [31] J. Kim, R. Godin, S. D. Dimitrov, T. Du, D. Bryant, M. A. McLachlan, J. R. Durrant, *Adv. Energy Mater.* **2018**, 8, 1802474.
- [32] H. Tan, A. Jain, O. Voznyy, X. Lan, F. P. Garcia de Arquer, J. Z. Fan, R. Quintero-Bermudez, M. Yuan, B. Zhang, Y. Zhao, F. Fan, P. Li, L. N. Quan, Y. Zhao, Z. H. Lu, Z. Yang, S. Hoogland, E. H. Sargent, *Science* **2017**, 355, 722.
- [33] Z. Liu, L. Krückemeier, B. Krogmeier, B. Klingebiel, J. A. Marquez, S. Levchenko, S. Öz, S. Mathur, U. Rau, T. Unold, T. Kirchartz, *ACS Energy Lett.* **2019**, 4, 110.
- [34] I. L. Braly, H. W. Hillhouse, *J. Phys. Chem. C* **2016**, 120, 893.
- [35] Reference Solar Spectral Irradiance: Air Mass 1.5, <http://rredc.nrel.gov/solar/spectra/am1.5/>, (accessed: April 2020).
- [36] P. Asbeck, *J. Appl. Phys.* **1977**, 48, 820.
- [37] J. Mattheis, J. H. Werner, U. Rau, *Phys. Rev. B* **2008**, 77, 085203.
- [38] J. Mattheis, *Mobility and Homogeneity Effects on the Power Conversion Efficiency of Solar Cells*, University Stuttgart, Stuttgart, Germany **2008**, p. 140.
- [39] M. Maiberg, T. Hölscher, S. Zahedi-Azad, R. Scheer, *J. Appl. Phys.* **2015**, 118, 105701.
- [40] E. M. Hutter, G. E. Eperon, S. D. Stranks, T. J. Savenije, *J. Phys. Chem. Lett.* **2015**, 6, 3082.
- [41] C. J. Hages, A. Redinger, S. Levchenko, H. Hempel, M. J. Koeper, R. Agrawal, D. Greiner, C. A. Kaufmann, T. Unold, *Adv. Energy Mater.* **2017**, 7, 1700167.
- [42] F. Zu, C. M. Wolff, M. Ralaiarisoa, P. Amsalem, D. Neher, N. Koch, *ACS Appl. Mater. Interfaces* **2019**, 11, 21578.
- [43] W. Shockley, W. T. Read, *Phys. Rev.* **1952**, 87, 835.
- [44] R. N. Hall, *Phys. Rev.* **1952**, 87, 387.
- [45] T. Kirchartz, *Philos. Trans. R. Soc., A* **2019**, 377, 20180286.
- [46] H. C. Casey, F. Stern, *J. Appl. Phys.* **1976**, 47, 631.
- [47] F. Stern, *J. Appl. Phys.* **1976**, 47, 5382.
- [48] J. H. Werner, J. Mattheis, U. Rau, *Thin Solid Films* **2005**, 480–481, 399.
- [49] T. Kirchartz, L. Krückemeier, E. L. Unger, *APL Mater.* **2018**, 6, 100702.
- [50] P. W. Bridgman, *Phys. Rev.* **1928**, 31, 101.
- [51] W. van Roosbroeck, W. Shockley, *Phys. Rev.* **1954**, 94, 1558.
- [52] J. M. Richter, M. Abdi-Jalebi, A. Sadhanala, M. Tabachnyk, J. P. H. Rivett, L. M. Pazos-Outon, K. C. Gödel, M. Price, F. Deschler, R. H. Friend, *Nat. Commun.* **2016**, 7, 13941.
- [53] F. Staub, T. Kirchartz, K. Bittkau, U. Rau, *J. Phys. Chem. Lett.* **2017**, 8, 5084.
- [54] T. Kirchartz, T. Markvart, U. Rau, D. A. Egger, *J. Phys. Chem. Lett.* **2018**, 9, 939.
- [55] T. Markvart, *Multiphonon Recombination*, Cambridge University Press, Cambridge, UK **2003**.
- [56] F. Staub, U. Rau, T. Kirchartz, *ACS Omega* **2018**, 3, 8009.
- [57] P. T. Landsberg, C. Rhys-Roberts, P. Lal, *Proc. Phys. Soc.* **1964**, 84, 915.
- [58] B. K. Ridley, *Solid-State Electron.* **1978**, 21, 1319.
- [59] B. K. Ridley, *J. Phys. C: Solid State Phys.* **1978**, 11, 2323.
- [60] K. Huang, A. Rhys, *Proc. R. Soc. London, Ser. A* **1950**, 204, 406.
- [61] T. Markvart, *Multiphonon Recombination*, Cambridge University Press, Cambridge, UK **2003**.
- [62] B. K. Ridley, *Quantum Processes in Semiconductors*, Oxford University Press, Oxford, UK **2013**.
- [63] J. S. Park, S. Kim, Z. Xie, A. Walsh, *Nat. Rev. Mater.* **2018**, 3, 194.
- [64] T. W. Crothers, R. L. Milot, J. B. Patel, E. S. Parrott, J. Schlipf, P. Müller-Buschbaum, M. B. Johnston, L. M. Herz, *Nano Lett.* **2017**, 17, 5782.
- [65] I. L. Braly, D. W. deQuilettes, L. M. Pazos-Outon, S. Burke, M. E. Ziffer, D. S. Ginger, H. W. Hillhouse, *Nat. Photonics* **2018**, 12, 355.
- [66] X. Zhang, J.-X. Shen, W. Wang, C. G. Van de Walle, *ACS Energy Lett.* **2018**, 3, 2329.
- [67] W. Shockley, H. J. Queisser, *J. Appl. Phys.* **1961**, 32, 510.
- [68] R. T. Ross, *J. Chem. Phys.* **1967**, 46, 4590.
- [69] T. Markvart, *Phys. Status Solidi A* **2008**, 205, 2752.
- [70] U. Rau, *Phys. Rev. B* **2007**, 76, 085303.
- [71] D. Luo, R. Su, W. Zhang, Q. Gong, R. Zhu, *Nat. Rev. Mater.* **2020**, 5, 44.
- [72] D. W. deQuilettes, K. Frohna, D. Emin, T. Kirchartz, V. Bulovic, D. S. Ginger, S. D. Stranks, *Chem. Rev.* **2019**, 119, 11007.
- [73] R. E. Brandt, J. R. Poindexter, P. Gorai, R. C. Kurchin, R. L. Z. Hoyer, L. Nienhaus, M. W. B. Wilson, J. A. Polizzotti, R. Sereika, R. Zaltauskas, L. C. Lee, J. L. MacManus-Driscoll, M. Bawendi, V. Stevanović, T. Buonassisi, *Chem. Mater.* **2017**, 29, 4667.
- [74] R. E. Brandt, V. Stevanović, D. S. Ginley, T. Buonassisi, *MRS Commun.* **2015**, 5, 265.
- [75] H. Jin, E. Debroye, M. Keshavarz, I. G. Scheblykin, M. B. J. Roeffaers, J. Hofkens, J. A. Steele, *Mater. Horiz.* **2020**.
- [76] A. Zakutayev, C. M. Caskey, A. N. Fioretti, D. S. Ginley, J. Vidal, V. Stevanovic, E. Tea, S. Lany, *J. Phys. Chem. Lett.* **2014**, 5, 1117.
- [77] M. V. Kovalenko, L. Protesescu, M. I. Bodnarchuk, *Science* **2017**, 358, 745.
- [78] M. H. Du, *J. Phys. Chem. Lett.* **2015**, 6, 1461.
- [79] Y. Rakita, I. Lubomirsky, D. Cahen, *Mater. Horiz.* **2019**, 6, 1297.
- [80] G. Smestad, H. Ries, *Sol. Energy Mater. Sol. Cells* **1992**, 25, 51.
- [81] U. Rau, B. Blank, T. C. M. Müller, T. Kirchartz, *Phys. Rev. Appl.* **2017**, 7, 044016.
- [82] U. Rau, U. W. Paetzold, T. Kirchartz, *Phys. Rev. B* **2014**, 90, 035211.
- [83] Y. Yang, M. Yang, D. Moore, Y. Yan, E. Miller, K. Zhu, M. Beard, *Nat. Energy* **2017**, 2, 16207.
- [84] D. W. deQuilettes, S. Koch, S. Burke, R. K. Paranjy, A. J. Shropshire, M. E. Ziffer, D. S. Ginger, *ACS Energy Lett.* **2016**, 1, 438.
- [85] S. G. Motti, D. Meggiolaro, A. J. Barker, E. Mosconi, C. A. R. Perini, J. M. Ball, M. Gandini, M. Kim, F. De Angelis, A. Petrozza, *Nat. Photonics* **2019**, 13, 532.

- [86] J. S. W. Godding, A. J. Ramadan, Y.-H. Lin, K. Schutt, H. J. Snaith, B. Wenger, *Joule* **2019**, *3*, 2716.
- [87] P. Würfel, *J. Phys. C: Solid State Phys.* **1982**, *15*, 3967.
- [88] P. Würfel, S. Finkbeiner, E. Daub, *Appl. Phys. A* **1995**, *60*, 67.
- [89] K. Schick, E. Daub, S. Finkbeiner, P. Würfel, *Appl. Phys. A* **1992**, *54*, 109.
- [90] G. Giorgi, J. I. Fujisawa, H. Segawa, K. Yamashita, *J. Phys. Chem. Lett.* **2013**, *4*, 4213.
- [91] J.-P. Yang, M. Meissner, T. Yamaguchi, X.-Y. Zhang, T. Ueba, L.-W. Cheng, S. Ideta, K. Tanaka, X.-H. Zeng, N. Ueno, S. Kera, *Sol. RRL* **2018**, *2*, 1800132.
- [92] T. Unold, L. Gutay, *Photoluminescence Analysis of Thin-Film Solar Cells*, Wiley, New York **2011**.
- [93] M. G. Abebe, A. Abass, G. Gomard, L. Zschiedrich, U. Lemmer, B. S. Richards, C. Rockstuhl, U. W. Paetzold, *Phys. Rev. B* **2018**, *98*, 075141.
- [94] T. Kirchartz, F. Staub, U. Rau, *ACS Energy Lett.* **2016**, *1*, 731.
- [95] P. Schulz, D. Cahen, A. Kahn, *Chem. Rev.* **2019**, *119*, 3349.
- [96] T. G. Allen, J. Bullock, X. Yang, A. Javey, S. De Wolf, *Nat. Energy* **2019**, *4*, 914.
- [97] H. Uratani, K. Yamashita, *J. Phys. Chem. Lett.* **2017**, *8*, 742.
- [98] S. H. Turren-Cruz, A. Hagfeldt, M. Saliba, *Science* **2018**, *362*, 449.
- [99] S. Gharibzadeh, B. Abdollahi Nejjand, M. Jakoby, T. Abzieher, D. Hauschild, S. Moghadamzadeh, J. A. Schwenzler, P. Brenner, R. Schmager, A. A. Haghighirad, L. Weinhardt, U. Lemmer, B. S. Richards, I. A. Howard, U. W. Paetzold, *Adv. Energy Mater.* **2019**, *9*, 1803699.
- [100] D. Luo, W. Yang, Z. Wang, A. Sadhanala, Q. Hu, R. Su, R. Shivanna, G. F. Trindade, J. F. Watts, Z. Xu, T. Liu, K. Chen, F. Ye, P. Wu, L. Zhao, J. Wu, Y. Tu, Y. Zhang, X. Yang, W. Zhang, R. H. Friend, Q. Gong, H. J. Snaith, R. Zhu, *Science* **2018**, *360*, 1442.
- [101] Q. Jiang, Y. Zhao, X. Zhang, X. Yang, Y. Chen, Z. Chu, Q. Ye, X. Li, Z. Yin, J. You, *Nat. Photonics* **2019**, *13*, 460.
- [102] T. Otaredian, *Solid-State Electron.* **1993**, *36*, 153.
- [103] A. B. Sproul, *J. Appl. Phys.* **1994**, *76*, 2851.
- [104] K. Bothe, R. Krain, R. Falster, R. Sinton, *Prog. Photovoltaics* **2010**, *18*, 204.
- [105] J. Tong, Z. Song, D. H. Kim, X. Chen, C. Chen, A. F. Palmstrom, P. F. Ndione, M. O. Reese, S. P. Dunfield, O. G. Reid, J. Liu, F. Zhang, S. P. Harvey, Z. Li, S. T. Christensen, G. Teeter, D. Zhao, M. M. Al-Jassim, M. F. A. M. van Hest, M. C. Beard, S. E. Shaheen, J. J. Berry, Y. Yan, K. Zhu, *Science* **2019**, *364*, 475.
- [106] D. Song, P. Cui, T. Wang, D. Wei, M. Li, F. Cao, X. Yue, P. Fu, Y. Li, Y. He, B. Jiang, M. Trevor, *J. Phys. Chem. C* **2015**, *119*, 22812.
- [107] S.-H. Turren-Cruz, M. Saliba, M. T. Mayer, H. Juárez-Santiesteban, X. Mathew, L. Nienhaus, W. Tress, M. P. Erodici, M.-J. Sher, M. G. Bawendi, M. Grätzel, A. Abate, A. Hagfeldt, J.-P. Correa-Baena, *Energy Environ. Sci.* **2018**, *11*, 78.
- [108] W. Nie, H. Tsai, R. Asadpour, J.-C. Blancon, A. J. Neukirch, G. Gupta, J. J. Crochet, M. Chhowalla, S. Tretiak, M. A. Alam, H.-L. Wang, A. D. Mohite, *Science* **2015**, *347*, 522.
- [109] E. A. Alharbi, M. I. Dar, N. Arora, M. H. Alotaibi, Y. A. Alzhrani, P. Yadav, W. Tress, A. Alyamani, A. Albadri, S. M. Zakeeruddin, M. Grätzel, *Research* **2019**, *2019*, 8474698.
- [110] S. Wu, Z. Li, J. Zhang, T. Liu, Z. Zhu, A. K. Y. Jen, *Chem. Commun.* **2019**, *55*, 4315.
- [111] S. Yang, J. Dai, Z. Yu, Y. Shao, Y. Zhou, X. Xiao, X. C. Zeng, J. Huang, *J. Am. Chem. Soc.* **2019**, *141*, 5781.
- [112] Q. Wang, E. Mosconi, C. Wolff, J. Li, D. Neher, F. De Angelis, G. P. Suranna, R. Grisorio, A. Abate, *Adv. Energy Mater.* **2019**, *9*, 1900990.
- [113] P. Caprioglio, F. Zu, C. M. Wolff, J. A. Márquez Prieto, M. Stollerfoht, P. Becker, N. Koch, T. Unold, B. Rech, S. Albrecht, D. Neher, *Sustainable Energy Fuels* **2019**, *3*, 550.
- [114] M. Abdi-Jalebi, Z. Andaji-Garmaroudi, S. Cacovich, C. Stavrakas, B. Philippe, J. M. Richter, M. Alsari, E. P. Booker, E. M. Hutter, A. J. Pearson, S. Lilliu, T. J. Savenije, H. Rensmo, G. Divitini, C. Ducati, R. H. Friend, S. D. Stranks, *Nature* **2018**, *555*, 497.
- [115] A. Al-Ashouri, A. Magomedov, M. Roß, M. Jošt, M. Talaikis, G. Chistiakova, T. Bertram, J. A. Márquez, E. Köhnen, E. Kasparavičius, S. Levenco, L. Gil-Escrig, C. J. Hages, R. Schlattmann, B. Rech, T. Malinauskas, T. Unold, C. A. Kaufmann, L. Korte, G. Niaura, V. Getautis, S. Albrecht, *Energy Environ. Sci.* **2019**, *12*, 3356.
- [116] M. Abdi-Jalebi, M. Ibrahim Dar, S. P. Senanayak, A. Sadhanala, Z. Andaji-Garmaroudi, L. M. Pazos-Outón, J. M. Richter, A. J. Pearson, H. Siringhaus, M. Grätzel, R. H. Friend, *Sci. Adv.* **2019**, *5*, eaav2012.
- [117] M. Abdi-Jalebi, M. Pazoki, B. Philippe, M. I. Dar, M. Alsari, A. Sadhanala, G. Divitini, R. Imani, S. Lilliu, J. Kullgren, H. Rensmo, M. Grätzel, R. H. Friend, *ACS Nano* **2018**, *12*, 7301.
- [118] A. W. Walker, S. Heckelmann, C. Karcher, O. Höhn, C. Went, M. Niemeyer, A. W. Bett, D. Lackner, *J. Appl. Phys.* **2016**, *119*, 155702.
- [119] S. Feldmann, S. Macpherson, S. P. Senanayak, M. Abdi-Jalebi, J. P. H. Rivett, G. Nan, G. D. Tainter, T. A. S. Doherty, K. Frohna, E. Ringe, R. H. Friend, H. Siringhaus, M. Saliba, D. Beljonne, S. D. Stranks, F. Deschler, *Nat. Photonics* **2020**, *14*, 123.